Journal of Advanced Research 75 (2025) 663–678

Contents lists available at ScienceDirect

Journal of Advanced Research

journal homepage: www.elsevier.com/locate/jare

Original Manuscript

# Cancer-associated fibroblasts regulate mitochondrial metabolism and inhibit chemosensitivity via ANGPTL4-IQGAP1 axis in prostate cancer

Zhi Xiong [a,b,c,1], Rui-Lin Zhuang [a,c,1], Shun-Li Yu [a,c], Zhao-Xiang Xie [a,c], Shi-Rong Peng [a,c], Ze-An Li [a,c], Bing-Heng Li [a,c], Jun-Jia Xie [a,c], Yi-Ning Li [d,*], Kai-Wen Li [a,c,e,*], Hai Huang [a,c,e,f,*]

[a] Department of Urology, Sun Yat-sen Memorial Hospital, Sun Yat-sen University, Guangzhou 510120, China
[b] Guangzhou First People's Hospital, The Second Affiliated Hospital of South China University of Technology, Guangzhou 510120, China
[c] Guangdong Provincial Key Laboratory of Malignant Tumor Epigenetics and Gene Regulation, Sun Yat-sen Memorial Hospital, Sun Yat-Sen University, Guangzhou 510120, China
[d] The Second Affiliated Hospital of Fujian Medical University, Quanzhou 362000, China
[e] Guangdong Provincial Clinical Research Center for Urological Diseases, Sun Yat-Sen Memorial Hospital, Sun Yat-Sen University, Guangzhou 510120, China
[f] Department of Urology, The Sixth Affiliated Hospital of Guangzhou Medical University, Qingyuan People's Hospital, Qingyuan 511518, Guangdong, China

## HIGHLIGHTS

- CAF promotes chemotherapy resistance in prostate cancer.
- CAFs promote mitochondrial biogenesis and OXPHOS metabolism in prostate cancer cells.
- CAFs paracrine ANGPTL4 binding to IQGAP1 on the PCa cell membrane activates Raf-MEK-ERK-PGC1α pathway.
- Specific inhibitors targeting IQGAP1 may enhance the responsiveness of prostate cancer to chemotherapy.

## GRAPHICAL ABSTRACT

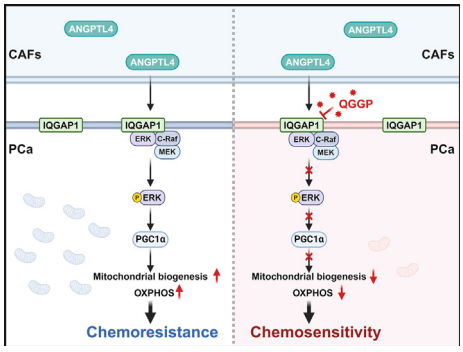


## ARTICLE INFO

*Article history:*
Received 23 September 2024
Accepted 3 December 2024
Available online 6 December 2024

*Keywords:*
ANGPTL4
Cancer-associated fibroblasts
Chemosensitivity
Mitochondria
Prostate cancer

## ABSTRACT

*Introduction:* Cancer-associated fibroblasts (CAFs) are a critical component of the tumor microenvironment, being implicated in enhancing tumor growth and fostering drug resistance. Nonetheless, the mechanisms underlying their function in prostate cancer (PCa) remain incompletely understood, which is essential for devising effective therapeutic strategies.
*Objectives:* The main objective of this study was to explore the mechanisms by which CAFs mediate PCa growth and chemoresistance.
*Methods:* We validated through data analysis and experimentation that CAFs significantly impact PCa cell proliferation and chemoresistance. Subsequently, we conducted a comprehensive proteomic analysis of the conditioned media from CAFs and PCa cells and identified angiopoietin-like protein 4 (ANGPTL4) as a key factor. We employed ELISA and multiplex immunofluorescence assays, all of which indicated that ANGPTL4 was primarily secreted by CAFs.Next, we conducted metabolomics analysis, GST pull-down assays, Co-IP, and other experiments to explore the specific molecular mechanisms of ANGPTL4 and its precise effects on PCa cells. Through drug screening, we identified Quercetin 3-O-(6′-galactopyranosyl)-β-D-galactopyranoside (QGGP) as an effective inhibitor of CAFs function. Finally, we thoroughly assessed the therapeutic potential of QGGP both as a monotherapy and in combination with docetaxel in PCa cells.

* Corresponding authors.
*E-mail addresses:* trocar@qq.com (Y.-N. Li), likw6@mail.sysu.edu.cn (K.-W. Li), huangh9@mail.sysu.edu.cn (H. Huang).
[1] These authors contributed equally to this work.

https://doi.org/10.1016/j.jare.2024.12.003
2090-1232/

*Results:* We discovered that the extracrine factor ANGPTL4 is primarily expressed in CAFs in PCa. When ANGPTL4 binds to IQ motif-containing GTPase-activating protein 1 (IQGAP1) on the PCa cell membrane, it activates the Raf-MEK-ERK-PGC1α axis, promoting mitochondrial biogenesis and OXPHOS metabolism, and thereby facilitating PCa growth and chemoresistance. Furthermore, virtual and functional screening strategies identified QGGP as a specific inhibitor of IQGAP1 that promotes its degradation. Combined with docetaxel treatment, QGGP can reverse the effects of CAFs and improve the responsiveness of PCa to chemotherapy.
*Conclusions:* This study uncovers a paracrine mechanism of chemoresistance in PCa and proposes that targeting the stroma could be a therapeutic choice.


## Introduction

Prostate cancer (PCa) stands as a widespread malignancy, ranking second among the leading causes of cancer-related fatalities in men [1]. While primary PCa initially responds well to androgen deprivation therapy (ADT), the majority of patients eventually progress to a castration-resistant stage (CRPC) with a poor prognosis [2]. A growing body of research indicates that the suppressive tumor microenvironment (TME) plays a pivotal role in driving the growth and drug resistance of various cancers, including the development of chemoresistant PCa [3]. Multiple factors and molecular events within the TME trigger signaling cascades in tumor cells, thereby contributing to the regulation of non-cell-autonomous drug resistance in cancer [4,5]. Therefore, gaining a deeper insight into the survival mechanisms of PCa cells is essential for improving patient outcomes.

Cancer-associated fibroblasts (CAFs) play a pivotal role in shaping the immunosuppressive microenvironment of PCa. The interstitial pressure generated by CAFs promotes PCa [6–8]. Recent studies have demonstrated the significance of metabolic reprogramming in the development, progression, and metastasis of PCa. Therefore, CAFs and tumor metabolism have become the focus of attention. Lactate secreted by CAFs can induce lipid metabolism reprogramming, enhancing the invasive ability of PCa cells [9]. CAFs induce metabolic reprogramming, specifically involving glutamine and cholesterol, in PCa cells. This reprogramming facilitates the development of resistance to androgen receptor (AR) targeted therapy in PCa [8,10]. Consequently, alterations in metabolism and energy adaptation likely play crucial roles in the progression and development of the PCa.

Mitochondria, the central hub of energy metabolism, are pivotal in tumor progression due to their role in coordinating cellular energy conversion processes like oxidative phosphorylation (OXPHOS), and they serve as significant markers of cancer [11,12]. Patients with PCa who exhibit severe mitochondrial phenotypes have shorter survival times [13]. Patients with PCa with high OXPHOS levels are less responsive to chemotherapy [14,15]. It is important to note that different tumors exhibit considerable metabolic heterogeneity. For example, patients with ovarian cancer with high OXPHOS levels are also less responsive to chemotherapy [16]. Exploring the mechanism utilized by PCa cells to harness metabolic pathways for tumor growth and survival, while simultaneously disrupting the crosstalk between tumors and stroma, bears significant scientific importance. Hence, we sought to explore the potential impact of CAFs on the progression of PCa through their influence on mitochondrial metabolism adaptation.

In this study, we combined molecular, cellular, genetic, metabolomic, and high-throughput virtual screening methods to reveal that CAFs promote PCa growth and chemoresistance by enhancing mitochondrial biogenesis and OXPHOS function, and proposed a corresponding combination therapy strategy to improve the sensitivity of PCa chemotherapy.

## Materials and methods

### *Cell culture*

The human PCa cell lines, including 22RV1, C4-2, LNCAP, VCAP, PC3, and DU145, were sourced from the CAS Center for Excellence in Molecular Cell Science located in Shanghai, China. Both normal fibroblasts (NFs) and CAFs were derived from PCa tumor tissues and their adjacent non-tumor counterparts. These cells were cultivated in RPMI-1640 medium (GIBCO, C11875500BT), enriched with 10% fetal bovine serum (FBS) (ExCell Bio, FSP500) and 1% penicillin–streptomycin (GIBCO, 15140–122). To ensure the absence of mycoplasma contamination, PCR analysis was conducted.

### *Pca specimens and isolation of primary fibroblasts*

Human PCa tissues, along with their corresponding normal prostate tissues located at a minimum distance of 5 cm from the tumor, were sourced from Sun Yat-sen Memorial Hospital, Sun Yat-sen University (Guangzhou, China). The Ethics Committee of Sun Yat-sen University's Sun Yat-sen Memorial Hospital approved the use of human specimens in this study. We obtained informed consent from the patients or their guardians, and none of the individuals had received any prior therapy. The PCa specimens were histopathologically diagnosed by two pathologists.

Fibroblasts were isolated using a previously described method [17]. Briefly, both tumor and non-tumor tissues underwent mincing and dissociation in RPMI-1640 medium enriched with 10% FBS and 0.5% collagenase Type I (Worthington, LS004197) for a duration of 2 h at 37 °C. The isolated fibroblasts were then cultivated in RPMI-1640 containing 10% FBS at 37 °C with 5% CO2 until they exhibited adherence to the culture dish.

The isolated cells were verified as CAFs based on several criteria: their spindle morphology, flow cytometric analysis revealing positivity for EPCAM-, CD45-, CD31-, and PDGFRα, and western blotting confirming increased expression of αSMA, FAP, Vimentin, and PDGFRα [18]. Fibroblasts were passaged below 6. One of the CAFs was transduced with the lenti-SV40 lentivirus for immortalization.

### *Conditioned media collection*

On the first day, NFs, CAFs, or human PCa cell lines were seeded into a 10 cm dish. The next day, cells underwent two washes with phosphate-buffered saline (PBS) before being replenished with serum-free media. On day three, conditioned media was gathered and replaced with fresh serum-free media. This process was repeated on day four. The collected conditioned media was then pooled together and filtered through a 0.45 μm filter (JET BIOFIL, FPE404030-1) to eliminate cellular debris. The resulting filtered

conditioned media could be stored at 4 °C for up to 7 days or at −80 °C for up to 3 months.

*Enzyme-linked immunosorbent assay*

The concentrations of ANGPTL4 were evaluated in conditioned media from CAFs, NFs, and human PCa cell lines using human ANGPTL4 ELISA kits (JIANG LAI, JL15325-96T) following the manufacturer's guidelines.

*qRT-PCR*

RNA extraction was performed using the RNA-Quick purification kit (ESscience, RN001) according to the manufacturer's guidelines. The extracted RNA was then diluted to below 500 ng/μL with DEPC-treated water. RT-PCR was carried out utilizing the qPCR SYBR Green Master Mix (Vazyme, Q711) in combination with the cDNA SuperMix kit (Vazyme, R333). The ABI Quanstudio DX Real-Time PCR System was employed to determine the mRNA expression levels of the target genes. For a comprehensive listing of all primers utilized in this study, please refer to Supplementary Table. S1.

*Western blot*

Cell lysates were prepared using RIPA Lysis Buffer (Beyotime, P0013B) containing 1% protease inhibitor cocktail (Cwbiotech, CW2200S) and 1% phosphatase inhibitor cocktail (Cwbiotech, CW2383S). Protein concentration was assessed with a BCA Protein Assay Kit (Beyotime, P0011) as per the manufacturer's directions. The proteins were subsequently mixed with 5x SDS-PAGE Protein Sample Loading Buffer (Beyotime, P0286), boiled at 95 °C for 10 min, and stored at −80 °C until further experimentation was required. Protein separation was achieved using cast gels (EpiZyme, PG112) alongside a Full-range Rainbow protein marker (Fisher Scientific, 26617), running the gels at 120v with a homemade 1x running buffer. For protein transfer, a homemade 1x transfer buffer and PVDF paper (Merck Millipore, ISEQ00010) were utilized, activating the paper with 100% methanol and conducting the transfer at 4 °C for 2 h at 250 mA. Following the transfer, the membrane was blocked with 5% nonfat milk for 1 h at 37 °C prior to the addition of the primary antibody. The membrane was incubated overnight at 4 °C with the suitable primary antibody (1:1000) diluted in TBST containing 5% BSA. After the incubation, the membrane underwent three washes with TBST, each lasting 30 min. It was then incubated for 1 h at 37 °C with horseradish peroxidase-linked goat anti-rabbit or anti-mouse IgG (1:3000). Following three additional 30-minute washes with TBST, the immunoblots were revealed using enhanced chemiluminescence. The antibodies used for the immunoblot assays were ANGPTL4 (1:1000; Proteintech, 18374–1-AP), PGC1α (1:1000; Proteintech, 66369–1-Ig), IQGAP1 (1:1000; Proteintech, 22167–1-AP), c-Raf (1:1000, Cell Signaling, 53745S), ERK (1:1000, ABclonal, A4782), P-ERK (1:1000; Proteintech, 28733–1-AP), MEK (1:1000; Proteintech, 11049–1-AP), NDUFB8 (1:1000, Abclonal, A19732), UQCRC2 (1:1000, Abclonal, A4366), ATP5A1 (1:1000, Abclonal, A11217), SDHB (1:1000, Abclonal, A1809), COX IV (1:1000, Abclonal, A6564), α-Tublin (1:1000, Proteintech, 11224–1-AP), and GAPDH (1:1000, Abclonal, A19056).

*Targeted TCA-cycle metabolomics*

For a period of 24 h, 22RV1 and LNCAP cells were exposed to both control medium and CAF-CM. The cell culture medium was aspirated and the cells were washed twice with 1 mL of ice-cold 0.9% PBS until the washings appeared colorless. The waste liquid was then discarded. Next, 1 mL of an ice-cold solution consisting of methanol, acetonitrile, and water in a 4:4:2 ratio (pre-cooled to −20 °C) was introduced. After ensuring even mixing, the cells were scraped off using a cell scraper and carefully transferred into a 1.5 mL EP tube. The resulting mixture was then vortexed at 37 °C for a duration of 10 min. The sample was centrifuged at 15,000 ×*g* for 10 min at 4 °C. The obtained supernatant (800 μL) was placed into a 1.5-mL EP tube and dried under vacuum at 4 °C. Prior to analysis, the sample was redissolved in 100 μL of a 50% acetonitrile–water solution. It was then centrifuged at 15,000 rpm for 5 min at 4 °C, and 80–100 μL of the supernatant was carefully transferred into a 2 mL mass spectrometer injection vial with an inner insert tube. The GC–MS measurements were conducted by the Bioinformatics and Omics Center at Sun Yat-sen Memorial Hospital, Sun Yat-sen University.

*Detection of citrate, malate, α-ketoglutarate(α-KG), succinate, and ATP levels*

The levels of citrate, malate, α-KG, succinate, and ATP were measured using the Citrate Assay Kit (Sigma-Aldrich, MAK333), Malate Assay Kit (Sigma-Aldrich, MAK067), α-KG Assay Kit (Sigma-Aldrich, MAK054), Succinate Assay Kit (Sigma-Aldrich, MAK335), and ATP Assay Kit (Beyotime, S0027), respectively. Briefly, 2 x $10^6$ PCa cells were subjected to treatment with control medium and CAF-CM for a duration of 24 h, followed by lysis using the corresponding detection buffer. Absorption, luminescence, and fluorescence were measured using a Multifunctional microplate detector (TECAN Spark10M) according to the manufacturer's guidelines.

*Mitochondrial DNA/nuclear DNA (mtDNA / nDNA) determination*

DNA extraction from the cells was performed utilizing the SteadyPure Universal Genomic DNA Extraction Kit (Accurate Biology, AG21009) in accordance with the manufacturer's guidelines. The extracted DNA was quantified and diluted to a concentration of less than 500 ng/mL. Equal amounts of DNA were utilized as templates to ascertain the relative copy numbers of mitochondrial DNA (cyclooxygenase-2, COX2) and nuclear DNA (Amyloid precursor protein, APP) via quantitative PCR. The ABI QuantStudio Sequence Detection System (Applied Biosystems) was employed in this process, along with the specific primer combinations listed in Supplementary Table. S1.

*Oxygen consumption rate (OCR) measurement*

OCR was determined using an Agilent Seahorse XFe96 Extracellular Flux Analyzer (Agilent Technologies, Santa Clara, CA, USA). 22RV1 and LNCAP cells (5 × $10^3$) were seeded overnight on specialized Seahorse tissue culture plates. Before the experiment, cells were washed and transferred to Seahorse assay medium containing 1 mM pyruvate, 2 mM glutamine, and 10 mM glucose. The cells were incubated in a non-$CO_2$ incubator at 37 °C for 1 h. After measuring the basal OCR level, the cell chamber received sequential injections of 1.5 μM oligomycin, 1.0 μM FCCP, and 0.5 μM antimycin/rotenone, following the XF Cell Mito Stress Test Kit protocol (Agilent, 103015–100). The basal OCR levels were calculated based on the area under the curve before oligomycin injection. OCR levels were calculated by measuring the AUC between FCCP and antimycin/rotenone injections.

*siRNA transient transfection*

To silence ANGPTL4, PGC1α, IQGAP1, and ERK, we performed RNA interference using specific siRNAs, along with a negative

control siRNA with no specific target. The siRNA oligonucleotides were acquired from GenePharma (Suzhou, China). Cells were transiently transfected with siRNA using Lipofectamine RNAiMAX (Invitrogen, 13778075), and the regular culture medium was substituted after 24 h. The efficacy of gene silencing was assessed by RT-PCR at 48 h post-transfection. For the target sequences of the siRNAs used in these experiments, please consult Supplementary Table. S2**.**

*GST pulldown assay*

The sequence of ANGPTL4 was cloned into a pGEX-6P-3 vector carrying a GST tag. Additionally, various regions of IQGAP1 were cloned into pGEX-4T-1 vectors to produce recombinant GST-tagged IQGAP1 protein constructs. These constructs encompassed specific amino acid ranges, namely IQGAP1-P1 (1–185), IQGAP1-P2 (166–670), IQGAP1-P3 (671–730), IQGAP1-P4 (731–860), IQGAP1-P5 (861–1250), and IQGAP1-P6 (1251–1657). The plasmids were transfected into E. coli and shaken at 37 °C for 10 h to amplify the protein. Afterward, 0.5mM isopropyl β-D-thiogalactoside (IPTG) (MedChemExpress, HY-15921) was added to the bacterial solution, which was then shaken and cultured for 6h at 37 °C. The bacteria were collected, and the fusion protein was prepared and purified using GST-tagged protein agarose beads (L-2004; Biolinkedin) following the manufacturer's instructions. The GST-ANGPTL4 protein was purified and mixed with membrane proteins from 22Rv1 or LNCAP. Likewise, the 6 GST-tagged IQGAP1 recombinant proteins were purified and mixed with CAFs proteins. The mixture was incubated overnight at 4 °C. Following washing, the proteins were separated via SDS-PAGE, stained with Coomassie blue, and analyzed using western blotting. Differential protein bands were then examined by mass spectrometry, which was performed at the Bioinformatics and Omics Center of Sun Yat-sen Memorial Hospital, Sun Yat-sen University.

*Coimmunoprecipitation (Co-IP) assays*

Cells were lysed on ice for 30 min using cell lysis buffer (APExBIO, K1123). After centrifugation, the supernatant was quantified, and equal protein amounts were incubated with the corresponding antibody at 4 °C overnight. The lysate was then incubated with protein A/G Magnetic Beads (Selleck, B23201) for 2 h at room temperature, followed by two washes with IP lysate. Elution buffer was added, and the beads were subsequently boiled at 95 °C for 10 min. Lastly, western blot analysis was performed.

*Immunofluorescence analysis*

Cells were seeded at approximately 60% confluence onto a cover glass (JET BIOFIL, BDD012035). Following a 24-hour incubation, the cellular samples were then prepared for subsequent analysis. BODIPY 493/503 (Proteintech, CM02294) was used to evaluate lipid droplets, whereas MitoTracker Red CMXRos (Beyotime, C1049B) was used to evaluate mitochondria, following the manufacturer's instructions. DAPI (Beyotime, C1006) or Hoechst (Beyotime, C1028) was used to label the cell nuclei. Fluorescence images were obtained using a ZEISS LSM710 laser scanning confocal microscope equipped with ZEN 2.3 software.

*Flow cytometric analysis*

In summary, PCa cells were labeled with MitoTracker Red CMXRos (Beyotime, C1049B) for 30 min at 37 °C. These cells were then treated with various compounds or a control vehicle, with DMSO serving as the drug vehicle at a final concentration not exceeding 0.1%. Following treatment, the cells were collected, stained with annexin V and DAPI, and analyzed using flow cytometry. A solution containing 1x annexin V binding buffer, fluorochrome-conjugated annexin V, and DAPI was added to the cells, which were incubated for 15 min at room temperature. All cells were subsequently analyzed using the Beckman CtoFLEX S system, and the data were processed with Beckman CtoFLEX S Software and FlowJo software v10.

*High-throughput virtual screening*

To identify potential inhibitors of IQGAP1, we used Schrödinger Maestro version 11.4 for structure-based High-throughput virtual screening (HTVS), the 3D drawing software PyMol, and the three-dimensional structure of human IQGA1 (AlphaFold ID: AFP46940-F1) from the Uniprot database. We hydrogenated the protein using the Protein Preparation Wizard module, followed by energy optimization (OPLS2005 force field, RMSD of 0.30 Å). A grid file was generated for the processed protein utilizing a receptor grid-generation module. The 2D formats of both the FDA-Approved Drug Library, consisting of 2700 compounds, and the MCE Bioactive Compound Library, comprising 16,600 compounds, were subjected to hydrogenation and energy optimization through the Schrödinger LigPrep Module. The resulting 3D structures were then outputted for virtual screening purposes.

For virtual screening, we utilized the Virtual Screening Workflow module, while the Glide module was employed for molecular docking. The receptor and ligand molecules were docked together based on geometric and energy matching criteria. The initial screening of 2,700 compounds in the FDA-Approved Drug Library was conducted using the Standard Precision (SP) mode. The top 20% of the molecules were selected based on their scoring values. The second round of screening was performed using the Extra Precision (XP) mode, which resulted in the ranking of small-molecule compounds. Meanwhile, the molecules from the MCE Bioactive Compound Library underwent screening using the HTVS mode within the Glide module. From this initial screening, the top 15% of molecules based on scoring values were chosen for further screening using the SP mode. Following this, the same top 15% of molecules were subjected to a third round of screening using the XP mode, ultimately yielding the final ranking of the small-molecule compounds. The top 200 compounds scored by both the FDA-Approved Drug Library and the MCE Bioactive Compound Library were manually reviewed for binding force between the target and the compound, as well as the compound structure. Among the screened compounds, the three molecules with the highest absolute docking scores were identified as candidates for subsequent experimental verification. These selected compounds are enumerated in Supplementary Table. S3. A higher absolute docking score predicts a stronger binding affinity between the molecule and the target. For both 2D and 3D mapping, the binding modes of the top-ranked drugs with IQGA1 were chosen for further analysis.

*Cellular thermal shift assay*

The 22RV1 and LNCAP cells were suspended in PBS containing a protease inhibitor cocktail and lysed by subjecting them to three freeze–thaw cycles with liquid nitrogen. The resulting cell lysate supernatant was centrifuged at 20,000 $\times g$ for 20 min to remove cell debris. The supernatant lysate was then divided into two subgroups: one was mixed with QGGP (200 μM), and the other served as the control group. After being mixed and incubated at 37 °C for 30 min, each group was divided equally into 8 PCR tubes. The tubes were then heated for 3 min in a thermal cycler (Bio-Rad, T100) at a specified temperature gradient of 50 to 85 °C to denature the protein, followed by cooling at 37 °C for 3 min. Next, SDS loading

buffer (Biosharp, BL502A) was added to the supernatant and inactivated at 95 °C for 10 min. Subsequently, 20 μL was taken, for western blotting with SDS-PAGE, and the cellular thermal shift assay (CETSA) curve was analyzed using GraphPad Prism software.

*Histology*

The tissues were preserved in 10% formalin for an entire night, following which they underwent the standard paraffin embedding procedure. This involved dehydration in ethanol, embedding in paraffin, and sectioning into 5 μm slices. These sections were then stored at ambient temperature. Staining with hematoxylin and eosin (HE) was carried out using the HE staining kit (Primary Biology, BH0001) in accordance with the manufacturer's guidelines.

For immunohistochemistry (IHC), the tissue sections underwent deparaffinization and rehydration using xylene and graded ethanol. Antigen retrieval was then performed by microwaving or autoclaving the sections in 0.1% sodium citrate buffer (pH 6.0) or Tris-EDTA (pH 8.0) for 20 min. Endogenous peroxidase activity was quenched with 3% H2O2, and non-specific binding was obstructed with a buffer containing 5% bovine serum albumin. The sections were incubated with the corresponding primary antibodies at 4 °C overnight. Following this, they were incubated with biotinylated secondary antibodies at a 1:200 dilution for 30 min, and subsequently with streptavidin-HRP at a 1:500 dilution for another 30 min. Visualization of the bound peroxidase was achieved by immersing the sections in a 3,3′-diaminobenzidine (DAB) solution (Powerful Biology, BH0053) for 1 to 10 min.

For immunofluorescence staining, the tissue sections underwent a series of preparation steps including deparaffinization, rehydration, antigen retrieval, and blocking. The primary EPCAM antibody was then added and allowed to incubate at 4 °C overnight. This was followed by the addition of the corresponding HRP-labeled secondary antibody and incubation at room temperature for 50 min. CY3-TSA was subsequently introduced and incubated in the dark at 37 °C for 10 min.The sections were placed in an EDTA repair solution (pH 8.0) within a repair box and subjected to microwave treatment. Afterward, the αSMA primary antibody was added and incubated at 4 °C overnight, followed by the addition of the corresponding HRP-labeled secondary antibody and incubation at room temperature for 50 min. FITC-TSA was then added and incubated in the dark at room temperature for an additional 10 min.Following microwave treatment, ANGPTL4 was introduced and incubated overnight at 4 °C. The sections were then exposed to a horseradish peroxidase-labeled secondary antibody and incubated at 37 °C for 50 min, prior to the addition of CY5-TSA and incubation at 37 °C for 10 min. The cell nuclei were counterstained with DAPI and allowed to incubate at room temperature for 10 min. Finally, fluorescent images were captured using a scanner (3DHISTECH Ltd., Pannoramic MIDI) and analyzed with CaseViewer software.

The following antibodies were used: Ki67 (1:500; Servicebio, GB111141), Cleaved caspase3 (1:500; Servicebio, GB11532), Caspase3 (1:500; Servicebio, GB11767C), αSMA (1:100; ABclonal, A17910), EPCAM (1:100; Cell Signaling, 14452S), ANGPTL4 (1:200; ABclonal, A2011), CY3-TSA (Powerful biology, BH0059), CY5-TSA (Powerful biology, BH0060), FITC-TSA (Powerful biology, BH0061).

*Blood biochemistry test*

Whole blood was collected by removing the mouse eyeball and left undisturbed at 37 °C for 2 h. The sample was then centrifuged at 800 ×*g* for 15 min at 4 °C. The supernatant was subsequently collected and assayed for levels of AST, ALT, BUN, and CRE using Rayto assay kits (R05602 for CRE, R02902 for BUN, R01702 for AST, and R01502 for ALT) in accordance with the provided operating instructions. The parameters were set using a fully automatic biochemistry instrument (Rayto, Chemray240), and the results were measured and exported automatically.

*Tumor xenografts*

A mixture of $2 \times 10^6$ 22RV1 cells, either alone or combined with an equal number of CAFs, was prepared in a 100 μL solution consisting of PBS and Matrigel (Corning, #354234) in a 1:1 ratio. This mixture was then administered subcutaneously to 4-week-old male nude BALB/c mice. Once the tumors reached approximately 100 $mm^3$ in size, the mice were randomly assigned to different groups for treatment. To investigate the impact of CAFs on DTX treatment, the mice were treated every three days with either a control solution (composed of 10% DMSO, 40% PEG300, 5% Tween80, and 45% ddH2O, administered intraperitoneally), DTX (5 mg/kg, intraperitoneally, from Selleck, S1148), QGGP (5 mg/kg, intraperitoneally, from MedChemExpress, HY-N7024), or a combination of DTX and QGGP. Tumor size (calculated using the formula V =engtth × $width^2$ × 0.5) and body weight were assessed every three days. On the 22nd day following the xenograft treatment, the animals were euthanized, and their tumors were collected for further analysis.

*Bioinformatic analyses and data mining*

Gene expression analysis in human PCa was conducted by utilizing gene profiling data from both the TCGA database (https://tcga-data.nci.nih.gov/tcga) and the GEO database, specifically employing the GSE193898 dataset (https://www.ncbi.nlm.nih.gov/geo/). Tumor stroke scores were calculated using the single-sample GSEA (ssGSEA) algorithm. The gene set used for the tumor stroke score calculation has been previously described [19]. Spearman correlation analysis was conducted using the TCGA database on Home for Researchers (https://www.home-for-researchers.com).

*Statistical methods*

To compare two groups, a two-tailed unpaired T test was employed, whereas for comparisons involving three or more groups, both one-way and two-way ANOVA tests followed by Tukey's multiple comparisons were utilized. All statistical analyses were conducted using GraphPad Prism (version 8.0). The quantified values are presented as mean ± SD, with statistical significance set at $P < 0.05$, denoted as follows: ns for no significance, * for $P < 0.05$, ** for $P < 0.01$, *** for $P < 0.001$, and **** for $P < 0.0001$.

## Results

*CAFs promote PCa growth*

Among all stromal cells in the TME, CAFs are the most abundant and are closely associated with cancer progression [20]. Then, we used CAFs isolated from human PCa tissues in our previous study [21], and collected conditional medium of CAFs (CAF-CM) for experiments. The results, as shown through plate cloning, indicate that CAF-CM significantly increased PCa cell proliferation (Fig. 1A). CCK8 cell proliferation analysis results showed that compared with the control group, CAF-CM significantly promoted the proliferation of LNCAP and 22RV1 cells (Fig. 1B). To confirm the effect of CAF on PCa *in vivo*, we subcutaneously co-transplanted CAFs with the PCa cell line 22RV1 into immunocompromised Nu/Nu mice. The growth rate of PCa in the CAFs group was significantly increased

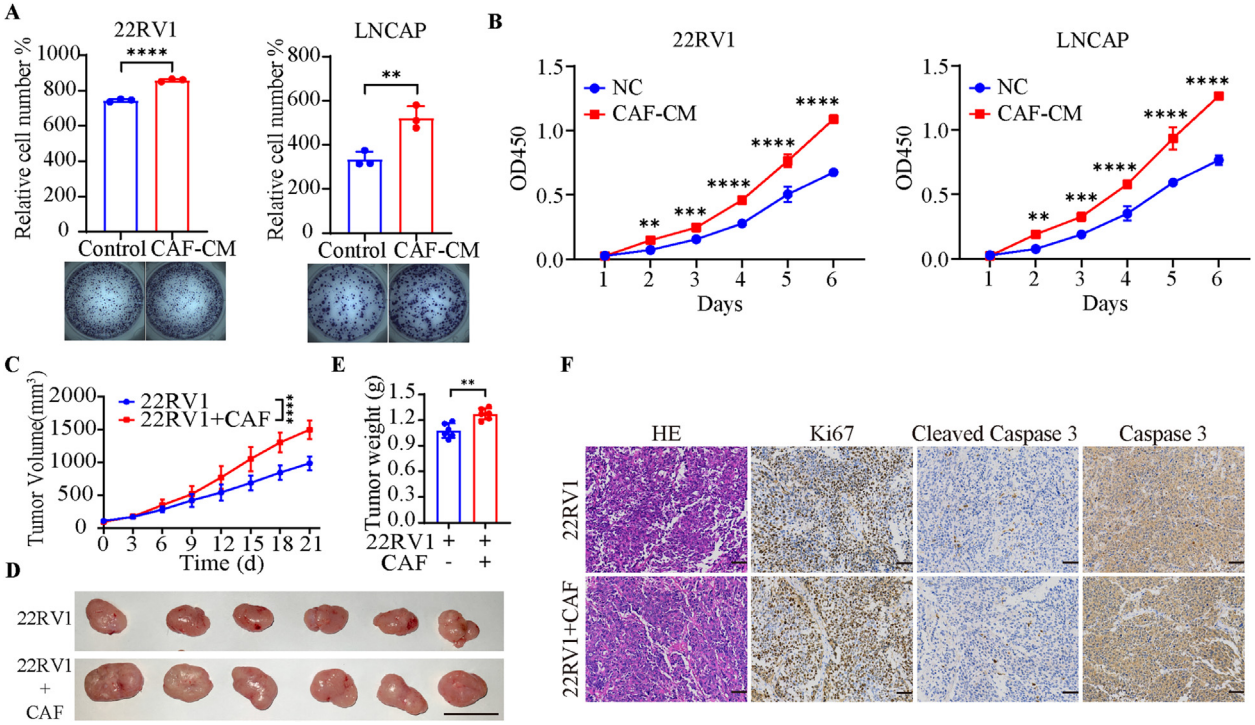


**Fig. 1. CAFs promote PCa cell proliferation. A.** Representative images and histogram analysis of colony formation assays betweenCAF-CM and control medium treated PCa cells (n = 3). **B.** CCK8 assays showing the proliferation of 22RV1 cells and LNCAP cells after culture with or without CAF-CM for the indicated days (n = 3). **C-E.** Representative volume (**C**), images (**D**), and size (**E**) of subcutaneous tumors formed after co-transplantation of 22RV1 cells with or without CAFs (n = 6). Scale bars, 1 c m. **F.** Representative H&E and IHC of the indicated proteins in tumors of the indicated groups. Scale bars, 20 μm. (*$P < 0.05$, **$P < 0.01$, ***$P < 0.001$, ****$P < 0.0001$).

(Fig. 1C). At the end of the experiment, the tumors were removed and weighed, and the tumor weight and tumor volume growth showed similar trends (Fig. 1D, E). To confirm the role of CAFs, we evaluated tumor sections using hematoxylin and eosin (HE) and immunohistochemical staining. Both the control and CAFs groups showed complete and compact tumor section structures, with no observable nuclear abnormalities (Fig. 1F). The IHC results indicated a significant increase in the proliferation marker Ki67 in the CAFs group compared to the control group, while the apoptosis marker Cleaved caspase 3 was significantly decreased in the CAFs group relative to the control group (Fig. 1F). In summary, the *in vitro* and *in vivo* experiments indicated that CAFs promote PCa growth.

### *CAFs promote mitochondrial content in PCa cells*

The Warburg effect, a metabolic shift from OXPHOS to aerobic glycolysis, is a phenomenon observed in various tumor types [22]. Although glycolysis increases, this does not necessarily preclude mitochondrial activity, thus not indicating a loss of mitochondrial function [23]. Mitochondrial genome variations are considered as potential biomarkers for the progression of various types of tumors [24,25]. A study found that the expression of mitochondrial content marker mitochondrially encoded cytochrome *c* oxidase II (MTCO2) was significantly correlated with tumor stage, Gleason grade, and lymph node metastasis in 11152 PCa specimens [26]. In addition, according to Kelly et al., their profiling of seven metabolic pathways in 404 patients with PCa revealed a significant upregulation of the OXPHOS pathway [27]. Meanwhile, recent studies have demonstrated that high-grade PCa exhibits a greater dependency on OXPHOS, and this shift in respiratory phenotype is strongly associated with tumor survival rates [13]. Accumulation of succinate, a metabolite of the mitochondrial TCA cycle, can also increase the malignancy of PCa cells [28]. These studies suggest that mitochondria play an important role in the progression of PCa.

To examine whether CAFs cause changes in mitochondrial energy metabolism in PCa cells, we examined several key intermediates in the mitochondrial TCA cycle. In PCa cells stimulated by CAF-CM, several key intermediates in the TCA cycle, such as citric acid, malic acid, alpha-ketoglutaric acid (α-KG), and succinic acid, were significantly increased (Fig. 2A, B). Furthermore, the generation of adenosine triphosphate (ATP) was notably elevated in PCa cells that were treated with CAF-CM (Fig. 2C). To assess the functional status of mitochondria in PCa cells promoted by CAFs, we observed a notable elevation in the mitochondrial oxygen consumption rate (OCR) upon stimulation of PCa cells with CAF-CM. Both the basal and maximum respiratory volumes exhibited a significant increase (Fig. 2D–I). This finding, combined with previous reports indicating the importance of OXPHOS in PCa progression, suggests that CAFs may rely on mitochondrial energy metabolism as a key metabolic strategy for PCa cell survival.

To further delineate specific alterations in mitochondria, transmission electron microscopy (TEM) was employed, revealing a notable increase in mitochondrial count within PCa cells following stimulation with CAF-CM (Fig. 2J), which is consistent with enhanced mitochondrial metabolism in PCa cells. Flow cytometry and immunofluorescence experiments using mitochondrial probes also confirmed that CAFs increase mitochondrial content in PCa cells (Fig. 2K, L, and Supplementary Fig. S1A, B). The mitochondrial content can be evaluated by determining the ratio of mitochondrial DNA (mtDNA) to nuclear DNA (nDNA) within cells. The mtDNA/nDNA ratio increased after CAF-CM stimulation of PCa cells (Supplementary Fig. S1C). Changes in mitochondrial mass and increases in ATP production through the electron transfer chain (ETC) occur during OXPHOS. The western blot revealed that the protein levels of the five respiratory complex subunits, NDUFB (I), SDHB (II), UQCRC2 (III), COXIV (IV), and ATP5A (V), increased significantly

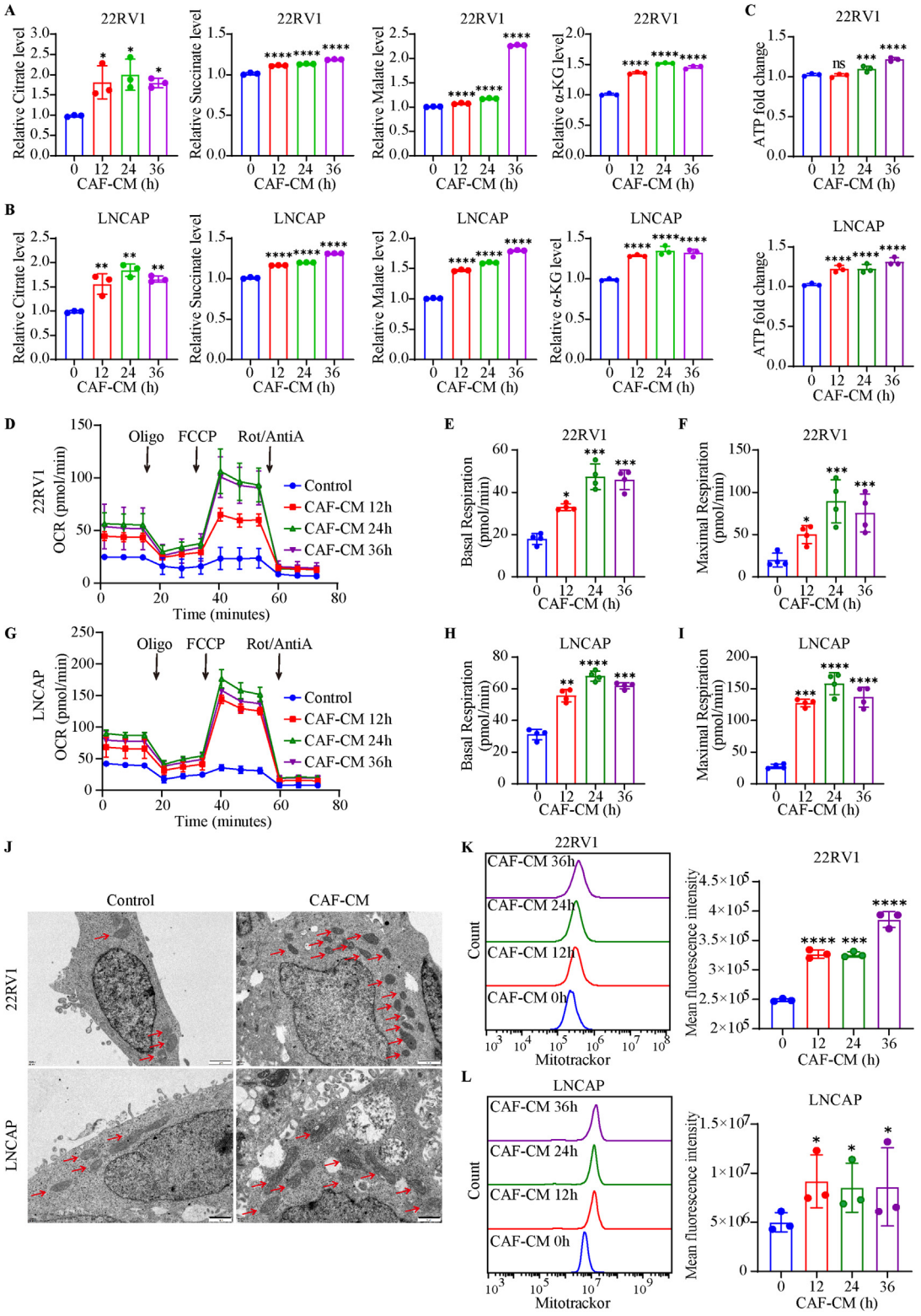


**Fig. 2. CAFs increase mitochondrial number and energy metabolism in PCa cells. A.B.** Changes in mitochondrial TCA cycle intermediate metabolites citrate, malate, succinate, and a-KG after CAF-CM stimulated 22RV1 **(A)** and LNCAP **(B)** cells for 12 h, 24 h, and 36 h (n = 3). **C.** Changes in OXPHOS product ATP after CAF-CM stimulated 22RV1 and LNCAP cells for 12 h, 24 h, and 36 h (n = 3). **D-I.** Mitochondrial OCR assay of control medium or CAF-CM treated 22RV1 and LNCAP cells. Oligo: Oligomycin, Rot/AntiA: Rotenone/antimycin A. Maximal respiration and spare respiratory capacity were interpolated from the time-course plot (n = 4). **J.** Representative TEM images of CAF-CM treated 22RV1 and LNCAP cells after 24 h. Scale bars, 1 μm. **K.L.** Flow cytometry was used to detect the number of mitochondria in 22RV1 and LNCAP after treatment with CAF-CM for 12 h, 24 h, and 36 h, and stained with MitoTracker Red (n = 3). (*$P < 0.05$, **$P < 0.01$, ***$P < 0.001$, ****$P < 0.0001$).

in ETC after CAF-CM stimulation of PCa cells (Supplementary Fig. S1D). The findings indicated that CAF-CM treatment elevated the mitochondrial content in PCa cells and augmented the function of OXPHOS.

*CAFs upregulate PGC1α expression and promote mitochondrial biogenesis in PCa cells*

Mitochondrial content is determined by the equilibrium between mitochondrial biogenesis, selective degradation of mitochondria, as well as mitochondrial fission and fusion processes [29]. However, following stimulation with CAF-CM, no significant alterations were observed in the expression of key genes involved in mitochondrial degradation, such as P62/SQSTM, PINK1, and NIX (Supplementary Fig. S2A, B). Similarly, no notable changes were detected in the expression of genes involved in the regulation of mitochondrial fusion and fission by CAFs, specifically OPA1, MFN1, and DRP1 (Supplementary Fig. S2A, B). Interestingly, we found that after CAF-CM stimulated PCa cells, the expression of the mitochondrial germinal gene PGC1α was significantly increased (Fig. 3A). Western blot also detected that CAFs significantly promoted PGC1α protein expression (Fig. 3B). Literature reports suggest that PGC1α, a protein responsible for controlling mitochondrial biogenesis, can influence changes in mitochondrial quality [30]. Therefore, we hypothesized that CAFs may regulate mitochondrial biogenesis through PGC1α. Knocking down PGC1α in PCa cells inhibited the promoting effect of CAFs on mitochondrial content (Fig. 3C, D; Supplementary Fig. S2C, D). Similarly,

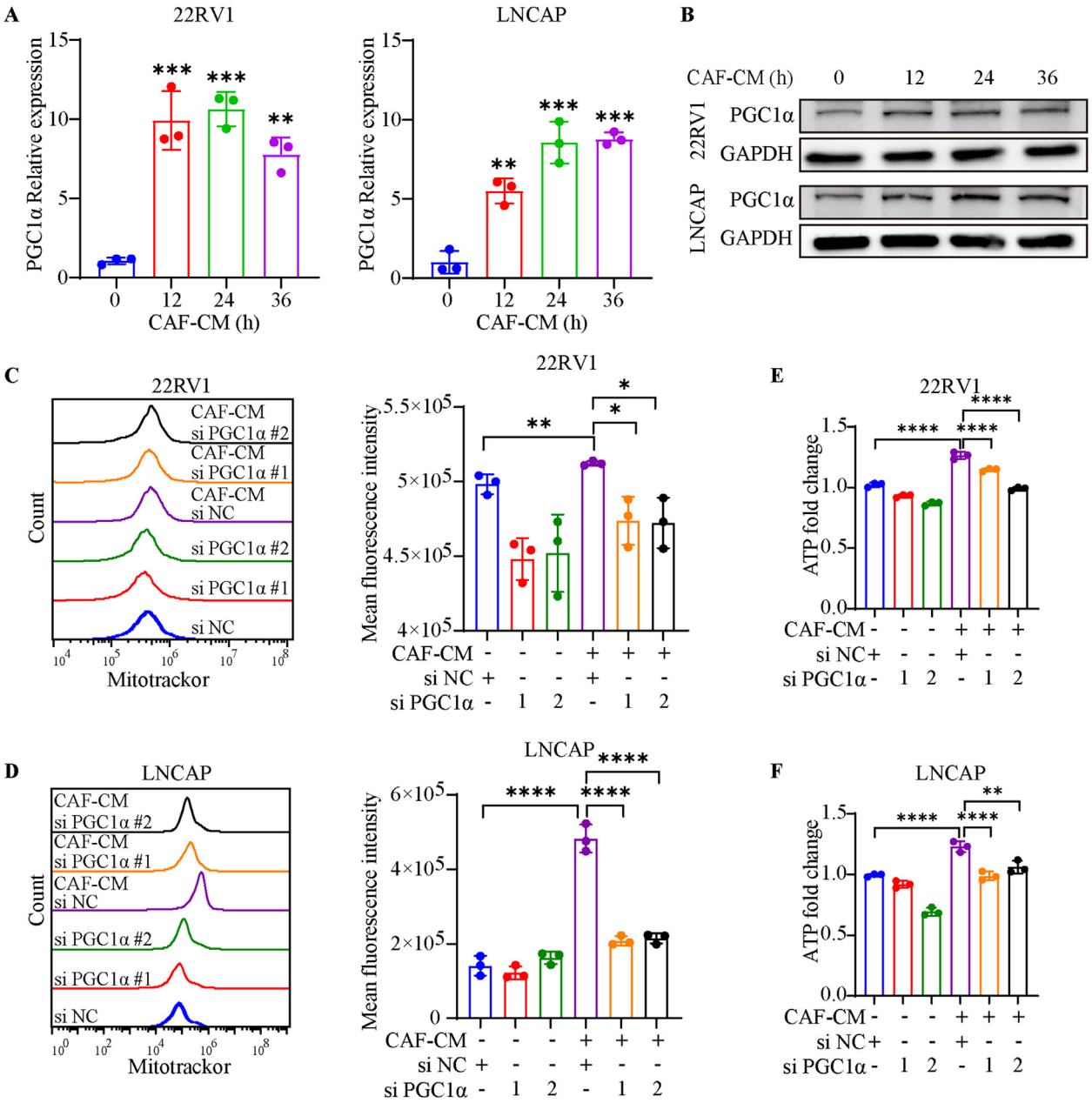


**Fig. 3. CAFs upregulated the expression of PGC1α and promoted mitochondrial biogenesis in PCa cells. A.** RT-PCR experiment demonstrates the expression of PGC1α in PCa cells treated with CAF-CM or control medium for 12 h, 24 h, and 36 h (n = 3). **B.** Representative western blot images of the PGC1α proteins in 22RV1 and LNCAP cells after treatment with CAF-CM for 12 h, 24 h, and 36 h. **C.D.** Number of mitochondria in PCa cells with PGC1α knockdown after treatment with CAF-CM or control medium for 24 h (n = 3). **E.F.** The ATP levels in PCa cells with PGC1α knockdown after treatment with CAF-CM or control medium for 24 h (n = 3). (*$P$ < 0.05, **$P$ < 0.01, ***$P$ < 0.001, ****$P$ < 0.0001).

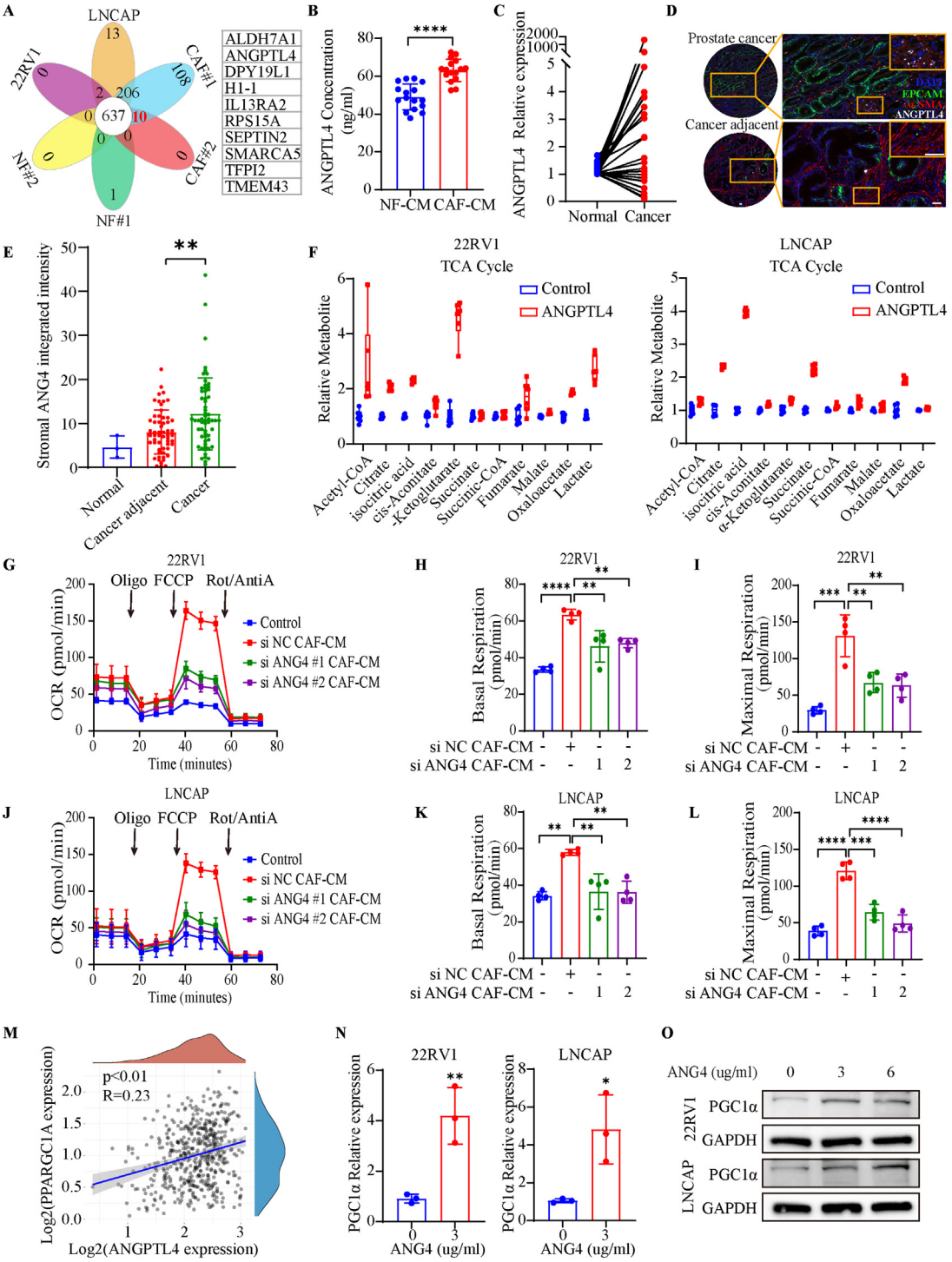


**Fig. 4. ANGPTL4 secreted by CAFs upregulates PGC1α expression to promote mitochondrial biogenesis in PCa cells. A.** Mass spectrometry results of conditioned media of PCa cells, NFs, and CAFs. **B.** ELISA of ANGPTL4 in the conditioned medium of paired NFs and CAFs (n = 16). **C.** The expression of ANGPTL4 in paired PCa and adjacent normal tissues was analyzed using RT-PCR (n = 30). **D.** Representative images of ANGPTL4 sources validated by the multichannel immunofluorescence method on PCa microarrays, including normal prostate tissue, PCa adjacent tissue, or PCa tissue samples. Epithelial tissue was labeled with EPCAM, and mesenchymal tissue was labeled with αSMA. Scale bars, 50 μm. **E.** Graphs depicting integrated intensities of stromal ANGPTL4 staining in normal prostate tissue (n = 3), PCa adjacent (n = 57), or PCa (n = 60) tissue. **F.** PCa cells were stimulated with control medium and recombinant ANGPTL4 for LC/MS analysis to assess TCA-cycle metabolites (n = 6). **G-L.** Mitochondrial OCR analysis of PCa cells with indicated treatments. CAF-CM from CAFs expressing siNC or siANGPTL4 was collected and added to PCa cells for 24 h. Oligo: Oligomycin, Rot/AntiA: Rotenone/antimycin A. Maximal respiration and spare respiratory capacity were interpolated from the time course plot (n = 4). **M.** Spearman correlation analysis between ANGPTL4 and PPARGC1A (PGC1α) in the TCGA cohort. **N.** RT-PCR detection of PGC1α expression in PCa cells stimulated with control medium or recombinant ANGPTL4 for 24 h (n = 3). **O.** Representative western blot images of the PGC1α in PCa cells stimulated with control medium and recombinant ANGPTL4 for 24 h. ANG4: ANGPTL4. (*$P$ < 0.05, **$P$ < 0.01, ***$P$ < 0.001, ****$P$ < 0.0001).

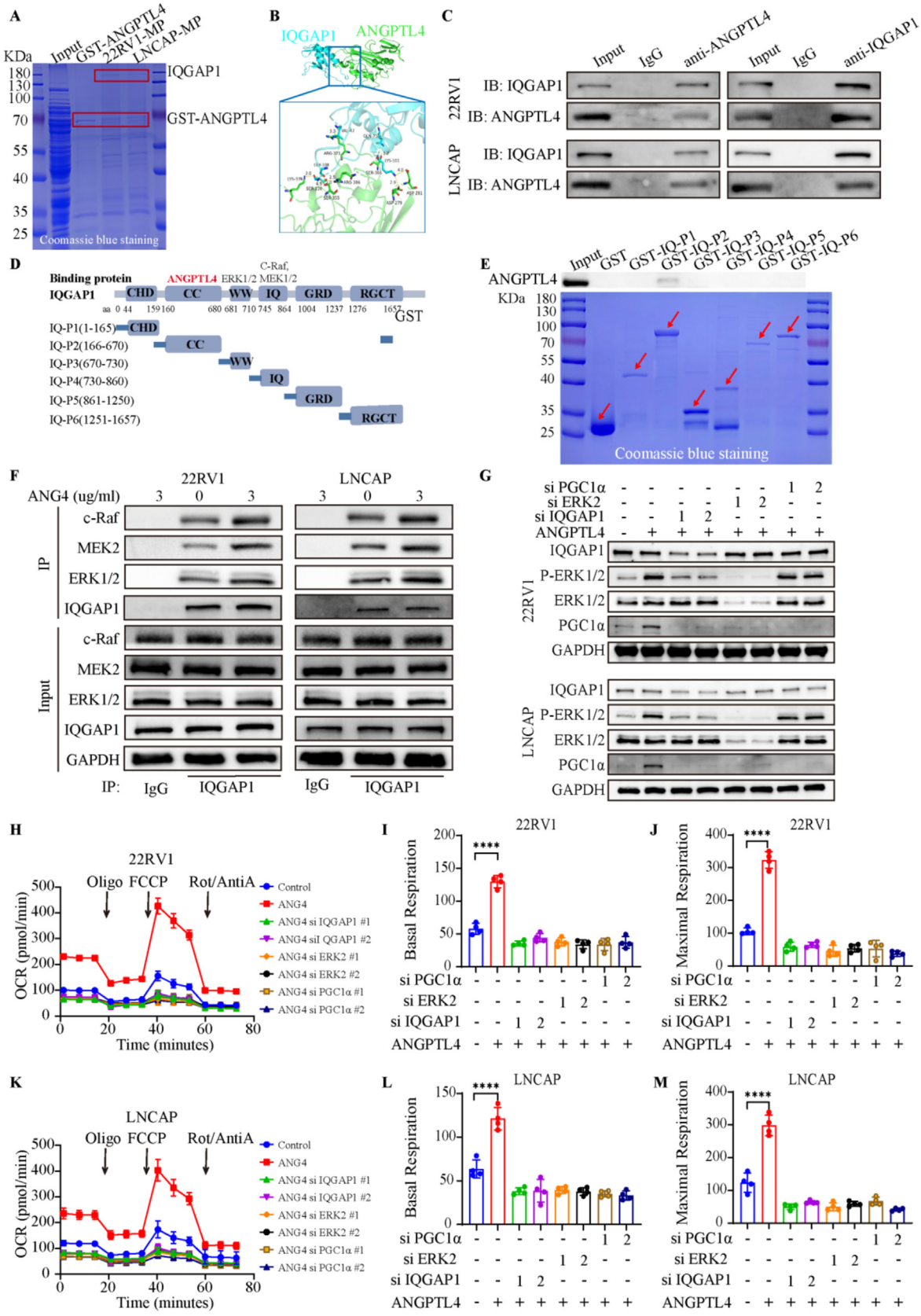
A
KDa
Input
GST-ANGPTL4
22RV1-MP
LNCAP-MP
180
130
100
70
55
40
35
25
IQGAP1
GST-ANGPTL4
Coomassie blue staining
B
IQGAP1
ANGPTL4
C
Input
IgG
anti-ANGPTL4
Input
IgG
anti-IQGAP1
22RV1
IB: IQGAP1
IB: ANGPTL4
LNCAP
IB: IQGAP1
IB: ANGPTL4
D
Binding protein
IQGAP1
C-Raf, ERK1/2 MEK1/2
ANGPTL4
CHD
CC
WW
IQ
GRD
RGCT
aa 0 44 159 160 680 681 710 745 864 1004 1237 1276 1652
GST
IQ-P1(1-165)
IQ-P2(166-670)
IQ-P3(670-730)
IQ-P4(730-860)
IQ-P5(861-1250)
IQ-P6(1251-1657)
E
Input
GST
GST-IQ-P1
GST-IQ-P2
GST-IQ-P3
GST-IQ-P4
GST-IQ-P5
GST-IQ-P6
ANGPTL4
KDa
180
130
100
70
55
40
35
25
Coomassie blue staining
F
22RV1
LNCAP
ANG4 (ug/ml)
3
0
3
3
0
3
IP
c-Raf
MEK2
ERK1/2
IQGAP1
Input
c-Raf
MEK2
ERK1/2
IQGAP1
GAPDH
IP:
IgG
IQGAP1
IgG
IQGAP1
G
si PGC1α
si ERK2
si IQGAP1
ANGPTL4
IQGAP1
P-ERK1/2
ERK1/2
PGC1α
GAPDH
22RV1
IQGAP1
P-ERK1/2
ERK1/2
PGC1α
GAPDH
LNCAP
H
22RV1
Oligo
FCCP
Rot/AntiA
OCR (pmol/min)
Time (minutes)
Control
ANG4
ANG4 si IQGAP1 #1
ANG4 siI QGAP1 #2
ANG4 si ERK2 #1
ANG4 si ERK2 #2
ANG4 si PGC1α #1
ANG4 si PGC1α #2
I
22RV1
Basal Respiration
****
si PGC1α
si ERK2
si IQGAP1
ANGPTL4
J
22RV1
Maximal Respiration
****
si PGC1α
si ERK2
si IQGAP1
ANGPTL4
K
LNCAP
Oligo
FCCP
Rot/AntiA
OCR (pmol/min)
Time (minutes)
Control
ANG4
ANG4 si IQGAP1 #1
ANG4 si IQGAP1 #2
ANG4 si ERK2 #1
ANG4 si ERK2 #2
ANG4 si PGC1α #1
ANG4 si PGC1α #2
L
LNCAP
Basal Respiration
****
si PGC1α
si ERK2
si IQGAP1
ANGPTL4
M
LNCAP
Maximal Respiration
****
si PGC1α
si ERK2
si IQGAP1
ANGPTL4

knocking down PGC1α in PCa cells also eliminated the role of CAFs in promoting ATP production (Fig. 3E, F). In summary, CAFs upregulate PGC1α expression and promote mitochondrial biogenesis in PCa cells.

*CAFs act on PCa cells through paracrine ANGPTL4*

To investigate the molecular regulatory mechanism of CAFs in PCa, we conducted mass spectrometric (MS) analysis on the conditioned medium of PCa cell lines (22RV1 and LNCAP), two pairs of adjacent normal fibroblasts (NFs) and CAFs (Fig. 4A). We found that 10 proteins were exclusively detected in the conditioned media of CAFs (Fig. 4A). Among these proteins, ANGPTL4 is closely associated with tumor metabolism [31,32]. Therefore, we hypothesize that CAFs may regulate PCa through ANGPTL4. Using an enzyme-linked immunosorbent assay (ELISA), we detected the expression of ANGPTL4 in the conditioned media of 16 pairs of NFs and CAFs. CAFs exhibited significantly higher levels of secreted ANGPTL4 compared to NFs (Fig. 4B). Further analysis of ANGPTL4 in the conditioned media of CAFs, NFs, and PCa cell lines (22RV1, LNCAP, VCAP, C4-2, DU145, and PC3) revealed that ANGPTL4 was mainly derived from CAFs (Supplementary Fig. S3A). Although ANGPTL4 expression was not observed in NFs and prostate cancer cells by mass spectrometry, this may be due to the relatively low selectivity and specificity of MS. To confirm our findings, we examined the expression of ANGPTL4 in 30 paired clinical samples of prostate cancer (PCa) and normal tissues. The results indicated that the expression of ANGPTL4 was significantly elevated in the tumor samples compared to the normal tissues (Fig. 4C). Furthermore, multicolor immunofluorescence detection of PCa chips revealed that ANGPTL4 was mainly expressed in CAFs (Fig. 4D). The expression of ANGPTL4 was found to be significantly higher in the stromal tissues of prostate cancer (PCa) compared to both adjacent and normal stromal tissues (Fig. 4E).

To further explore whether ANGPTL4 can mimic the role of CAFs in PCa. Targeted TCA-cycle metabolomics testing revealed that the recombinant protein ANGPTL4 promotes a significant increase in TCA-cycle metabolites in PCa cells (Fig. 4F). To determine if ANGPTL4 mimics the function of CAFs in promoting mitochondrial biogenesis, relevant experiments were conducted. The results indicate that ANGPTL4 increased the number of mitochondria (Supplementary Fig. S3B, C) and significantly promoted an increase in the proteins of the five respiratory complex subunits of ETC (Supplementary Fig. S3D). The mitochondrial respiration experiments further confirmed that the effect of ANGPTL4 on PCa cells is similar to that of CAFs. Specifically, ANGPTL4 promoted mitochondrial OCR and increased ATP production in PCa cells (Supplementary Fig. S3E-J). The above results suggest that ANGPTL4 exhibits similar functions to CAFs.

Through rescue experiments, we confirmed that CAFs mainly exert their function in PCa by secreting ANGPTL4. Knocking down ANGPTL4 in CAFs using siRNA significantly reduced the expression and secretion of ANGPTL4 from CAFs (Supplementary Fig. S4A, B). The decrease in ANGPTL4 expression significantly inhibited the promotion of mitochondrial content by CAFs in PCa cells (Supplementary Fig. S4C, D). Furthermore, after inhibiting the expression of ANGPTL4 in CAFs, the stimulatory effect of CAFs on mitochondrial OCR (Fig. 4G-L) and ATP production (Supplementary Fig. S4E, F) in PCa cells was significantly inhibited.

To investigate whether the specific mechanism by which ANGPTL4 exerts its function is consistent with CAFs. A significant correlation was found between ANGPTL4 and PGC1α through Spearman correlation analysis conducted on PCa data from the The Cancer Genome Atlas (TCGA) database (Fig. 4M). Moreover, we confirmed through RT-PCR and WB experiments that ANGPTL4 promotes the expression of PGC1α (Fig. 4N, O). These findings establish that ANGPTL4 plays a regulatory role in the expression of PGC1α in PCa. In summary, our study confirms that CAFs promote mitochondrial biogenesis and energy metabolism of PCa through paracrine ANGPTL4.

*ANGPTL4 binds to IQGAP1 on the PCa cell membrane and activates the ERK pathway*

To investigate the specific molecular mechanisms downstream of ANGPTL4, we hypothesized that ANGPTL4 acts on the cell membranes of tumor cells in its secreted form. To test this hypothesis, we constructed a GST-ANGPTL4 plasmid and performed GST pull-down experiments using the cell membrane proteins of 22RV1 and LNCAP cells (Fig. 5A). Mass spectrometry analysis revealed proteins in differential bands, including ANGPTL4 (bait) and a significant amount of bound IQ motif-containing GTPase-activating protein 1 (IQGAP1) (Fig. 5A; Supplementary Fig. S5A). Therefore, we additionally investigated the interaction between ANGPTL4 and IQGAP1. Molecular docking analysis revealed the formation of eight hydrogen bonds between the IQGAP1 and ANGPTL4 proteins, resulting in a binding energy of −247.33 kcal/mol, ensuring the stable combination of the two proteins (Fig. 5B; Supplementary Fig. S5B). The mutual binding between endogenous ANGPTL4 and IQGAP1 in 22RV1 and LNCAP cells was confirmed by coimmunoprecipitation (Co-IP) experiments (Fig. 5C). To identify the specific domain of IQGAP1 that interacts with ANGPTL4, six distinct GST-IQGAP1 recombinant proteins, each representing a different functional segment of IQGAP1, were generated (Fig. 5D, E). GST pulldown experiments revealed that the coiled-coil domain of IQGAP1 specifically interacts with ANGPTL4 (Fig. 5E).

IQGAP1 serves as a crucial scaffolding protein that plays a key role in the activation of the Raf-MEK-ERK signaling pathway and is tightly linked to tumor progression [33,34]. Consistent with previous studies, IQGAP1 interactions with c-Raf, MEK, and ERK were detected in 22RV1 and LNCAP cells, and ANGPTL4 significantly enhanced IQGAP1 interactions with them (Fig. 5F). These data

**Fig. 5. ANGPTL4 activates the Raf-MEK-ERK pathway by binding to IQGAP1 on the membrane of PCa cells to exert its function. A.** 22RV1 and LNCAP cell membrane lysates were subjected to a GST pulldown assay by GST-ANGPTL4 recombinant proteins. MP: membrane protein. **B.** 3D diagram of molecular docking analysis of the ANGPTL4-IQGAP1 interaction. The green ribbon structure represents ANGPTL4 protein, and the blue ribbon structure represents IQGAP1 protein. The stick structures represent interacting amino acid residues, and the yellow dashed line represents hydrogen bonding. **C.** Western blot detection of co-immunoprecipitated endogenous ANGPTL4 and IQGAP1 proteins in PCa cells. **D.** Schematic structural representation of IQGAP1 and six GST-IQGAP1 domains. CC, coiled-coil domain. **E.** CAFs whole cell lysates were subjected to GST pulldown experiments using GST or six recombinant GST-IQGAP1 proteins, and western blot analysis was performed for the ANGPTL4 protein. Red arrows indicate proteins with expected molecular weights. **F.** Western blot analysis of input and Co-IP samples in PCa cells stimulated with control medium or recombinant ANGPTL4 for 24 h. **G.** IQGAP1, ERK, and PGC1α in PCa cells were knocked down by siRNA, and treated with recombinant ANGPTL4 (3 ug/ml). The indicated proteins were determined using western blot. **H-M.** Mitochondrial OCR analysis of PCa cells when siRNA was used to knock down IQGAP1, ERK, and PGC1α, followed by treatment with recombinant ANGPTL4. ligo: Oligomycin, Rot/AntiA: Rotenone/antimycin A. Maximal respiration and spare respiratory capacity were interpolated from the time course plot (n = 4). NC, negative control. (*$P$ < 0.05, **$P$ < 0.01, ***$P$ < 0.001, ****$P$ < 0.0001).

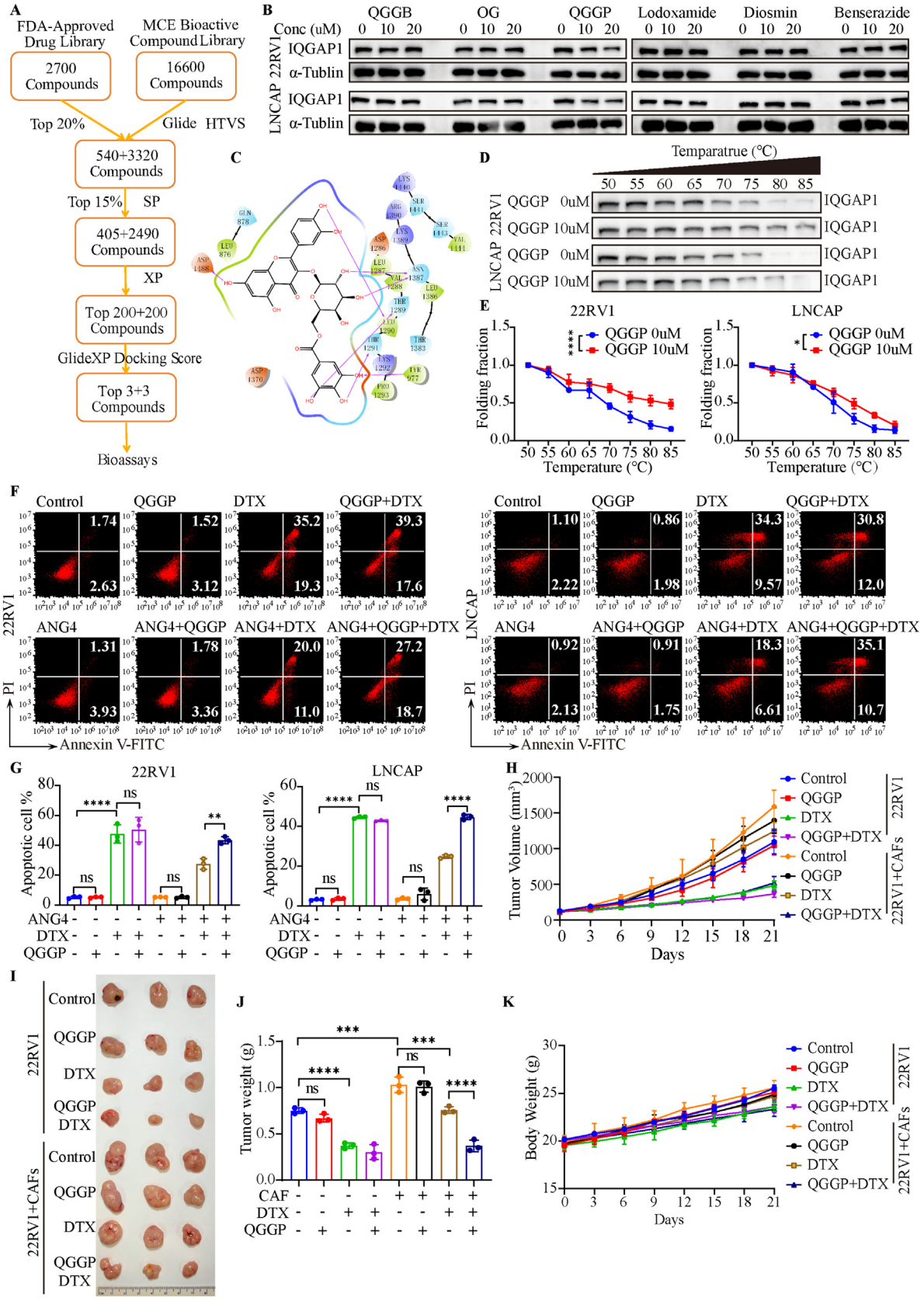
A
FDA-Approved Drug Library
MCE Bioactive Compound Library
2700 Compounds
16600 Compounds
Top 20%
Glide HTVS
540+3320 Compounds
Top 15%
SP
405+2490 Compounds
XP
Top 200+200 Compounds
GlideXP Docking Score
Top 3+3 Compounds
Bioassays
B
QGGB
OG
QGGP
Lodoxamide
Diosmin
Benserazide
Conc (uM) 0 10 20
LNCAP 22RV1
IQGAP1
α-Tublin
C
D
Temparatrue (°C)
50 55 60 65 70 75 80 85
QGGP 0uM
QGGP 10uM
IQGAP1
E
22RV1
LNCAP
Folding fraction
QGGP 0uM
QGGP 10uM
Temperature (°C)
F
Control
QGGP
DTX
QGGP+DTX
ANG4
ANG4+QGGP
ANG4+DTX
ANG4+QGGP+DTX
22RV1
LNCAP
PI
Annexin V-FITC
1.74
1.52
35.2
39.3
2.63
3.12
19.3
17.6
1.10
0.86
34.3
30.8
2.22
1.98
9.57
12.0
1.31
1.78
20.0
27.2
3.93
3.36
11.0
18.7
0.92
0.91
18.3
35.1
2.13
1.75
6.61
10.7
G
22RV1
LNCAP
Apoptotic cell %
ANG4
DTX
QGGP
H
Tumor Volume (mm³)
Days
Control
QGGP
DTX
QGGP+DTX
22RV1
22RV1+CAFs
I
22RV1
22RV1+CAFs
Control
QGGP
DTX
QGGP DTX
J
Tumor weight (g)
CAF
K
Body Weight (g)
Days

suggest that ANGPTL4 promotes PGC1α expression by activating the ERK pathway after binding to IQGAP1. By knocking down IQGAP1, ERK2, and PGC1α with siRNA, we observed a reduction in the activation of their respective downstream mediators (Fig. 5G; Supplementary Fig. 5C, D). The mitochondrial OCR of PCa cells promoted by ANGPTL4 was significantly inhibited after knocking down IQGAP1, ERK2, and PGC1α (Fig. 5H–M). In addition, after knocking down IQGAP1, ERK2 and PGC1α in PCa cells, the increase in ATP promoted by ANGPTL4 was also significantly inhibited (Supplementary Fig. 5E, F).

Collectively, our findings imply that ANGPTL4 interacts with IQGAP1 located on the cell membrane of PCa, triggering the activation of the cRAF-MEK-ERK-PGC1α signaling cascade. This process subsequently mediates mitochondrial biogenesis and facilitates the reprogramming of energy metabolism in PCa cells.

### *IQGAP1 inhibitor QGGP combined with DTX treatment improves the effect of PCa chemotherapy*

Paclitaxel and its semisynthetic analog docetaxel (DTX) are commonly used as front-line chemotherapy agents for the treatment of solid tumors. However, preclinical research has shown that the activation of the Ras-Raf-MAPK signaling pathway can contribute to the development of resistance against paclitaxel [35–37]. Furthermore, it has been observed that variations in the mitochondrial genome are linked to drug resistance in PCa, highlighting the significance of mitochondrial alterations in the development of therapeutic resistance [38]. PCa undergoes a metabolic shift from glycolysis to OXPHOS during the process of acquiring chemoresistance [15], and inhibiting the mitochondrial OXPHOS process significantly reduces the survival rate of drug-resistant PCa cells [15,39]. We then investigated whether enhanced mitochondrial OXPHOS function affects the sensitivity of DTX. We conducted a galactose sensitivity assay on PCa cells in the control medium and CAF-CM. When glucose in the culture medium is replaced by galactose (4.5 g/L), cells can only produce ATP through mitochondrial OXPHOS. We found that PCa cells treated with CAF-CM survive more in galactose medium, and PCa cells with enhanced OXPHOS function have decreased sensitivity to DTX, manifesting as decreased apoptosis (Supplementary Fig. S6A, B) and increased cell viability (Supplementary Fig. S6C, D), confirming that the enhanced mitochondrial OXPHOS inhibits the chemotherapy sensitivity of PCa. These studies and experimental results suggest that OXPHOS is also important for the development of treatment resistance in PCa. In addition, studies have found that CAFs also play an important role in the process of tumor [40]. Studies have indicated that CAF) can contribute to the development of resistance against endocrine therapy in PCa [6,41]. However, the precise mechanism by which CAFs may contribute to chemotherapy resistance in PCa remains elusive at present. Given that CAFs promote mitochondrial biogenesis through the Ras-Raf-ERK pathway in PCa, we speculate that CAFs may be involved in the process of chemoresistance in PCa.

Further analysis of TCGA dataset of PCa revealed a significant increase in the tumor stromal score in drug-treated PCa (Supplementary Fig. S7A). The tumor stromal score showed a positive correlation with the Gleason score (Supplementary Fig. S7B). Patients with higher tumor stromal scores had a worse prognosis after receiving therapy (Supplementary Fig. S7C). However, there was no correlation between prognosis and tumor stromal scores in patients who did not receive therapy (Supplementary Fig. S7D). The tumor stromal score of the PCa chemotherapy samples in TCGA was significantly higher than in the untreated group (Supplementary Fig. S7E). Analysis of paired data before and after chemotherapy for PCa revealed a significant increase in the tumor stroma score after chemotherapy (Supplementary Fig. S7F). Furthermore, the survival ratio of PCa cells treated with DTX was significantly increased after co-culture with CAF-CM (Supplementary Fig. S7G, H). Further observation of the apoptotic response to DTX showed that co-culture with CAF-CM significantly reduced the apoptotic ratio of 22RV1 and LNCAP cells after DTX treatment (Supplementary Fig. S7I, J). These findings suggest that CAFs contribute to chemotherapy resistance in PCa.

To address the clinical challenge of chemoresistance in PCa caused by CAFs, we further explored the combination of targeting the ANGPTL4-IQGAP1 axis in CAFs to improve the efficacy of chemotherapy. Due to the absence of commercially available inhibitors targeting IQGAP1, we performed a structure-based high-throughput virtual screening (HTVS) on 19,300 compounds sourced from the FDA and MCE activity libraries. This screening process aimed to identify potential inhibitors of IQGAP1 (Fig. 6A). The three compounds with the highest docking scores in the two libraries were selected for further experimental verification (Fig. 6A). The three compounds in the FDA libraries are Lodoxamide, Diosmin and Benserazide respectively, and the three compounds in the MCE activity libraries are Quercetin-3-O-β-D-glucose-7-O-β-D-gentiobiosiden (QGGP), QGGP and 2″-O-Galloylhyperin (OG) respectively (Supplementary Table. S3). QGGP exhibited the strongest inhibitory effect on IQGAP1 protein expression (Fig. 6B). According to computer docking, QGGP could form seven hydrogen bonds with IQGAP1. Five phenolic hydroxyl groups could form five hydrogen bonds with ASP1488, LEU1290, TYR977, THR1289, and THR1291. Furthermore, two hydroxyl groups on the sugar ring could form two hydrogen bonds with ASN1387 (Fig. 6C; Supplementary Fig. S8A). A Cellular Thermal Shift Assay (CETSA) was performed to determine the direct interaction between QGGP and IQGAP1 proteins. The results showed that QGGP caused significant changes in the thermal stability of IQGAP1 in 22RV1 and LNCAP cells (Fig. 6D, E).

We found that ANGPTL4 secreted by CAFs significantly inhibited the sensitivity of PCa cells to DTX (Fig. 6F, G). Although QGGP alone had no significant effect on PCa cells, it significantly inhibited the function of ANGPTL4 and enhanced the anti-tumor effect of DTX on PCa cells (Fig. 6F, G). *In vivo* experiments have demonstrated that the combination of QGGP and DTX effectively suppresses the role of CAFs in promoting chemoresistance in PCa,

**Fig. 6. IQGAP1 inhibitor QGGP enhances the chemosensitivity of PCa. A.** Workflow of HTVS for IQGAP1 inhibitor identification. **B.** Western blot analysis of IQGAP1 expression in PCa cells treated by the top three inhibitors showing the strongest binding ability in the FDA-Approved Drug Library and MCE Bioactive Compound Library for 24 h. **C.** The chemical structure and molecular docking model of the binding between QGGP and the human IQGAP1 protein. QGGP forms seven hydrogen bonds with IQGAP1: the five phenolic hydroxyl groups can form five hydrogen bonds with ASP1488, LEU1290, TYR977, THR1289, and THR1291, and the two hydroxyl groups on the sugar ring can form two hydrogen bonds with ASN1387. **D. E.** Cellular thermal shift assay was used to determine the effect of QGGP on IQGAP1 protein stability (n = 3). **F. G.** Apoptosis analysis of PCa cells with indicated treatments. PCa cells were pretreated with QGGP (10 μM) or DMSO for 1 h, followed by control medium or recombinant ANGPTL4 (3 ug/ml). Apoptosis analyses were performed 24 h after DTX treatment (n = 3). **H.** The volume of tumors in the indicated groups, measured every 3 days (n = 3). **I. J.** Representative images and sizes of subcutaneous tumors formed by human 22RV1 cells co-transplanted with or without CAFs into BALB/C-nude mice and treated with control, DTX, QGGP, or combination (n = 3). **K.** The body weight in the indicated groups, measured every 3 days (n = 3). (*$P$ < 0.05, **$P$ < 0.01, ***$P$ < 0.001, ****$P$ < 0.0001).

and this combined treatment significantly hinders tumor growth (Fig. 6H-J). The proliferation indicator Ki67 and the apoptosis indicator cleaved caspase 3 showed the same trend (Supplementary Fig. S8B). To evaluate the *in vivo* safety of QGGP combined with DTX treatment, blood samples and major organs were collected from the treated mice at the conclusion of the study. The HE staining results indicated that the mice exhibited no apparent organic changes or inflammatory damage after receiving the combined treatment (Supplementary Fig. S8C). Moreover, blood biochemical analyses were conducted, encompassing liver function indicators such as aspartate aminotransferase (AST) and alanine aminotransferase (ALT), as well as renal function markers including blood urea nitrogen (BUN) and creatinine (CRE). The results revealed no statistically significant differences among the groups (Supplementary Fig. S8D). No significant weight loss was observed in either group (Fig. 6K). These findings confirm that the combined treatment had no significant toxic side effects on the liver, kidneys, or other organs, and was safe for *in vivo* use.

## Disscusion

PCa is resistant to current treatments due to the tumor's inherent heterogeneity and the immunosuppressive TME [6–9]. In PCa research, stromal CAFs play a crucial role in regulating the TME and promoting tumor growth, metastasis, and treatment resistance. Therefore, CAFs have become an important target for cancer treatment [6,8,41–44]. Studies have also shown that CAFs may affect key tumor characteristics, such as the regulation of tumor metabolic reprogramming [8] and the promotion of PCa progression. The study confirms the correlation between CAFs, tumor metabolism, and drug resistance. It suggests that CAFs in the microenvironment regulate tumor metabolism by secreting ANGPTL4, which becomes a core driver of PCa chemotherapy resistance.

Alterations in mitochondrial dynamics, biogenesis, and metabolism are significant factors in the progression of various pathophysiological conditions. For instance, mitochondrial fission can promote the self-renewal of human PCa stem-like tumor cells [45], and increased mitochondrial mass is associated with the progression of pancreatic cancer [46]. Furthermore, epigenetic modifications of mtRNA may serve as therapeutic targets against tumor metastasis [47]. Simultaneously, PCa cells acquire functional mitochondria from CAFs through intercellular tunnels, promoting PCa growth [48]. Studies have shown that PCa has a higher burden of deleterious mitochondrial DNA (mtDNA) mutations, indicating a greater reliance on mitochondrial oxidative metabolism and increased succinate oxidation during tumor progression [13]. Large-scale cohort studies have found that mitochondrial content and OXPHOS pathway in PCa are significantly related to clinical progression [26,27]. Therefore, reprogramming of energy metabolism and mitochondrial adaptation are believed to play a role in PCa progression. Previous studies have primarily focused on cell-autonomous mechanisms, neglecting he contribution of TME to the adaptive changes in tumor metabolism.

This study identified ANGPTL4 as a potential therapeutic target in the PCa microenvironment. ANGPTL4 belongs to the angiopoietin family and is a multifunctional protein that plays a crucial role in various metabolic and non-metabolic diseases [49]. It is widely recognized for its involvement in amino acid and lipid metabolism [50–52], inflammation, angiogenesis [53], and tumorigenesis [32]. Therefore, ANGPTL4 plays a central role in energy metabolism and

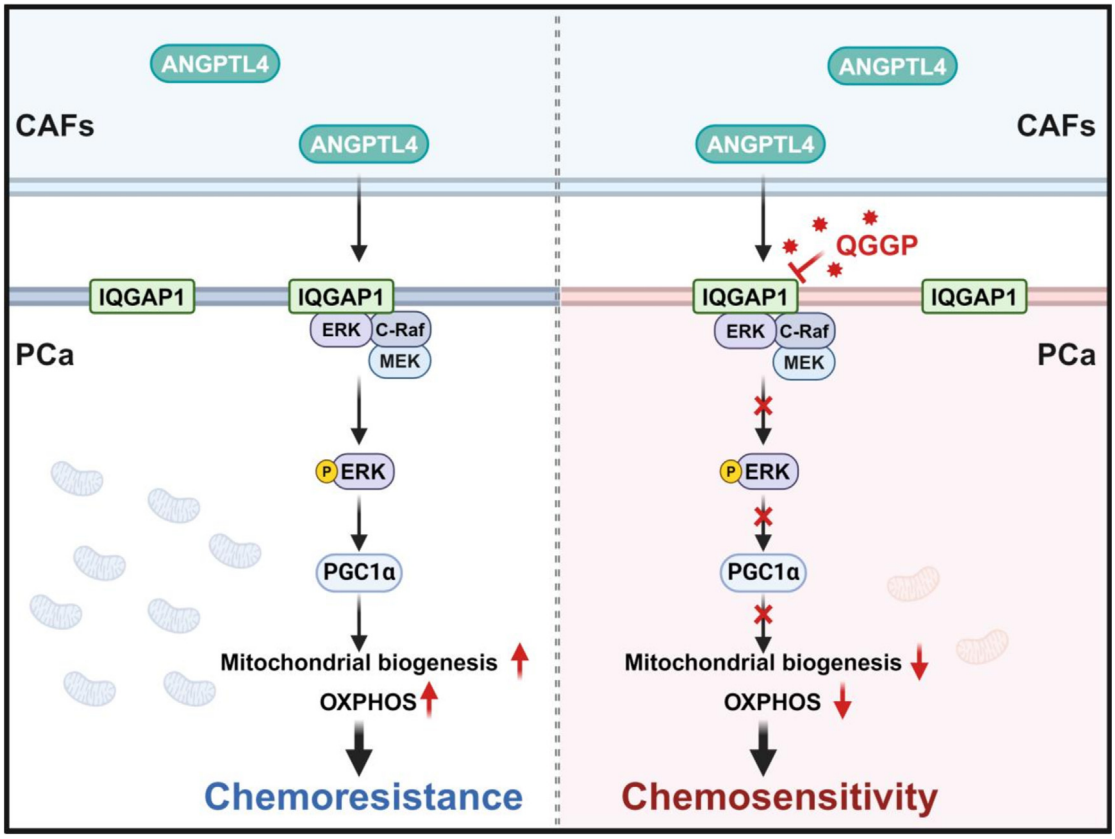


**Fig. 7. Schematic diagram of CAF-mediated chemoresistance in PCa**. CAFs paracrine ANGPTL4 binds to IQGAP1 on the PCa cell membrane, activates the Raf-MEK-ERK-PGC1α pathway, PGC1α mediates mitochondrial biogenesis and OXPHOS enhancement, thereby promoting PCa chemotherapy resistance (left). The IQGAP1-specific inhibitor QGGP blocks the effect of CAFs and improves the response to chemotherapy in PCa (right).

tumor progression. During epithelial-mesenchymal transition (EMT), ANGPTL4 provides metabolic flexibility to cancer cells, ensuring sufficient cellular energy and conferring EMT-mediated chemotherapy resistance [31]. Furthermore, ANGPTL4 expression was significantly high in CAFs of breast and ovarian cancer [54,55]. Although some studies suggest that ANGPTL4 may serve as a clinical biomarker and therapeutic target for human PCa [51], research on the specific source and mechanism of ANGPTL4 in human PCa remains limited. Our findings indicate that ANGPTL4 is primarily derived from CAFs in human PCa. Moreover, we also found that IQGAP1 is a new receptor of ANGPTL4. IQGAP1 is a scaffolding protein that regulates the extracellular signal-regulated kinase (RAS-ERK) pathway, it can assemble components of different kinase layers into a continuous phosphorylation cascade [55]. At the same time, studies have shown that the activation of ERK signaling pathway promotes the chemoresistance of PCa [33]. This study found that ANGPTL4 secreted by CAFs combines with IQGAP1 to activate the phosphorylated ERK pathway. This activation may promotes the expression of Ca(+)/cAMP-response element binding protein (CREB), which promotes the expression of PGC1α [56]. PGC1α is a mitochondrial germinal gene that promotes mitochondrial biogenesis [30]. Mitochondrial biogenesis enhances OXPHOS function, leading to chemoresistance in PCa. Through HTVS, we discovered that QGGP is a potential inhibitor of IQGAP1. It directly interacts with the IQGAP1 protein to inhibit its expression. The combined administration of QGGP and DTX synergistically inhibited PCa growth and induced cell death. Thus, the interaction between ANGPTL4 and IQGAP1 presents a potential target for sensitization to chemotherapy for PCa. This provides a theoretical basis for understanding the role of the stroma in the development of PCa, and targeting the stroma may be a reliable therapeutic option.

While our study offers preclinical insights in anticipation of the human trial, it is acknowledged that certain limitations persist. A potential concern is that using only the subcutaneous model as a single animal model poses a challenge to the efficacy of our proposed combination therapy model. Therefore, the treatment strategy of QGGP combined with DTX still needs more model validation. In addition, we have not yet addressed the specific reasons for the upregulation of ANGPTL4 in CAFs, and clarifying this mechanism may be more helpful in addressing chemotherapy resistance in PCa. In the future, we will focus on research on this scientific issue.

## Conclusions

This study revealed a significant correlation between PCa stroma and therapeutic resistance, especially chemoresistance. This research demonstrated that ANGPTL4 is primarily expressed in CAFs and that ANGPTL4 can bind to IQGAP1 on the PCa cell membrane, activating the Raf-MEK-ERK-PGC1α pathway. This process promotes mitochondrial biogenesis and OXPHOS function, ultimately leading to growth and chemoresistance in PCa. Then we found QGGP, a specific inhibitor of IQGAP1, through high-throughput virtual screening combined with functional validation, and QGGP significantly inhibited the role of CAFs (Fig. 7). These findings support the design of future clinical trials of IQGAP1 inhibitors combined with chemotherapy to treat patients with PCa, considering the safety of combination therapy.

## Compliance with Ethics Requirements.

All animal experiments were approved by the Animal Ethics Committee of Sun Yat-sen University (SYSU-IACUC-2021–000041) and performed in accordance with the guidelines of the Animal Care and Use Committee of Sun Yat-sen University. Experiments using human tissues were approved by the Ethics Committee of Sun Yat-Sen Memory Hospital (SYSEC-KY-KS-2020–201).

## Declaration of competing interest

The authors declare that they have no known competing financial interests or personal relationships that could have appeared to influence the work reported in this paper.

## Acknowledgements

This work was supported by the Key R&D Plan of Guangdong Province (No: 2023B1111030006); National key R&D plan of China (No: 2022YFC3602904); National Natural Science Foundation of China (No: 81974395, No: 82173036); International Science and technology cooperation project plan of Guangdong Province (No: 2021A0505030085); Sun Yat-Sen University Clinical Research 5010 Program (No: 2019005); Beijing Bethune Charitable Foundation (No: mnzl202001); Guangzhou Science and Technology Key R&D Project (No: 202206010117); Beijing Xisike Clinical Oncology Research Foundation (No: Y-MSDZD2022-0760, No: Y-tongshu2021/ms-0162); Joint funds for the innovation of science and technology, Fujian province (No: 2023Y9228); Supported by the open research funds from the Sixth Affiliated Hospital of Guangzhou Medical University, Qingyuan People's Hospital to Hai Huang.

This study was supported by the National Natural Science Foundation of China (No: 82173088), Natural Science Foundation of Guangdong (No: 2022A1515012383), the Guangzhou Science and Technology Fund (No: A202201011299), Baiqiuen Fund, Fundamental Research Funds for the Central Universities, Sun Yat-sen University to Kaiwen Li.

## Appendix A. Supplementary data

Supplementary data to this article can be found online at https://doi.org/10.1016/j.jare.2024.12.003.

## References

[1] Siegel RL, Miller KD, Wagle NS, Jemal A. Cancer statistics, 2023. CA Cancer J Clin 2023;73(1):17–48.
[2] Cai M, Song XL, Li XA, Chen M, Guo J, Yang DH, et al. Current therapy and drug resistance in metastatic castration-resistant prostate cancer. Drug Resist Updat 2023;68:100962.
[3] Luo Y, Liang H. Single-cell dissection of tumor microenvironmental response and resistance to cancer therapy. Trends Genet 2023;39(10):758–72.
[4] Qu Y, Dou B, Tan H, Feng Y, Wang N, Wang D. Tumor microenvironment-driven non-cell-autonomous resistance to antineoplastic treatment. Mol Cancer 2019;18(1):69.
[5] Chhabra Y, Weeraratna AT. Fibroblasts in cancer: Unity in heterogeneity. Cell 2023;186(8):1580–609.
[6] Zhang Z, Karthaus WR, Lee YS, Gao VR, Wu C, Russo JW, et al. Tumor microenvironment-derived NRG1 promotes antiandrogen resistance in prostate cancer. Cancer Cell 2020;38(2):279–96 e9.
[7] Cui D, Li J, Zhu Z, Berk M, Hardaway A, McManus J, et al. Cancer-associated fibroblast-secreted glucosamine alters the androgen biosynthesis program in prostate cancer via HSD3B1 upregulation. J Clin Invest 2023;133(7).
[8] Mishra R, Haldar S, Placencio V, Madhav A, Rohena-Rivera K, Agarwal P, et al. Stromal epigenetic alterations drive metabolic and neuroendocrine prostate cancer reprogramming. J Clin Invest 2018;128(10):4472–84.
[9] Ippolito L, Comito G, Parri M, Iozzo M, Duatti A, Virgilio F, et al. Lactate rewires lipid metabolism and sustains a metabolic-epigenetic Axis in prostate cancer. Cancer Res 2022;82(7):1267–82.
[10] Neuwirt H, Bouchal J, Kharaishvili G, Ploner C, Johrer K, Pitterl F, et al. Cancer-associated fibroblasts promote prostate tumor growth and progression through upregulation of cholesterol and steroid biosynthesis. Cell Commun Signal 2020;18(1):11.
[11] Pavlova NN, Thompson CB. The emerging hallmarks of cancer metabolism. Cell Metab 2016;23(1):27–47.
[12] Pavlova NN, Zhu J, Thompson CB. The hallmarks of cancer metabolism: still emerging. Cell Metab 2022;34(3):355–77.

[13] Schopf B, Weissensteiner H, Schafer G, Fazzini F, Charoentong P, Naschberger A, et al. OXPHOS remodeling in high-grade prostate cancer involves mtDNA mutations and increased succinate oxidation. Nat Commun 2020;11(1):1487.
[14] Yang Y, Qin H, Ding M, Ji C, Chen W, Diao W, et al. Small ankyrin 1 (sANK1) promotes docetaxel resistance in castration-resistant prostate cancer cells by enhancing oxidative phosphorylation. FEBS Open Bio 2023;13(2):257–69.
[15] Ippolito L, Marini A, Cavallini L, Morandi A, Pietrovito L, Pintus G, et al. Metabolic shift toward oxidative phosphorylation in docetaxel resistant prostate cancer cells. Oncotarget 2016;7(38):61890–904.
[16] Gentric G, Kieffer Y, Mieulet V, Goundiam O, Bonneau C, Nemati F, et al. PML-regulated mitochondrial metabolism enhances chemosensitivity in human ovarian cancers. Cell Metab 2019;29(1):156–73 e10.
[17] Sharon Y, Alon L, Glanz S, Servais C, Erez N. Isolation of normal and cancer-associated fibroblasts from fresh tissues by Fluorescence Activated Cell Sorting (FACS). J Vis Exp 2013;71:e4425.
[18] Xiong Z, Yu SL, Xie ZX, Zhuang RL, Peng SR, Wang Q, et al. Cancer-associated fibroblasts promote enzalutamide resistance and PD-L1 expression in prostate cancer through CCL5-CCR5 paracrine axis. iScience 2024;27(5):109674.
[19] Tyekucheva S, Bowden M, Bango C, Giunchi F, Huang Y, Zhou C, et al. Stromal and epithelial transcriptional map of initiation progression and metastatic potential of human prostate cancer. Nat Commun 2017;8(1):420.
[20] Chen X, Song E. Turning foes to friends: targeting cancer-associated fibroblasts. Nat Rev Drug Discov 2019;18(2):99–115.
[21] Xiong Z, Yu S-L, Xie Z-X, Zhuang R-L, Peng S-R, Wang Q, et al. Cancer-associated fibroblasts promote enzalutamide resistance and PD-L1 expression in prostate cancer through CCL5-CCR5 paracrine axis. iScience 2024:109674.
[22] Potter M, Newport E, Morten KJ. The Warburg effect: 80 years on. Biochem Soc Trans 2016;44(5):1499–505.
[23] DeBerardinis RJ, Chandel NS. We need to talk about the Warburg effect. Nat Metab 2020;2(2):127–9.
[24] Lu J, Sharma LK, Bai Y. Implications of mitochondrial DNA mutations and mitochondrial dysfunction in tumorigenesis. Cell Res 2009;19(7):802–15.
[25] Kalsbeek AMF, Chan EKF, Corcoran NM, Hovens CM, Hayes VM. Mitochondrial genome variation and prostate cancer: a review of the mutational landscape and application to clinical management. Oncotarget 2017;8(41):71342–57.
[26] Grupp K, Jedrzejewska K, Tsourlakis MC, Koop C, Wilczak W, Adam M, et al. High mitochondria content is associated with prostate cancer disease progression. Mol Cancer 2013;12(1):145.
[27] Kelly RS, Sinnott JA, Rider JR, Ebot EM, Gerke T, Bowden M, et al. The role of tumor metabolism as a driver of prostate cancer progression and lethal disease: results from a nested case-control study. Cancer Metab 2016;4:22.
[28] Sant'Anna-Silva ACB, Perez-Valencia JA, Sciacovelli M, Lalou C, Sarlak S, Tronci L, et al. Succinate anaplerosis has an onco-driving potential in prostate cancer cells. Cancers (Basel) 2021;13(7).
[29] Zhang C, Gao X, Li M, Yu X, Huang F, Wang Y, et al. The role of mitochondrial quality surveillance in skin aging: Focus on mitochondrial dynamics, biogenesis and mitophagy. Ageing Res Rev 2023;87:101917.
[30] Bennett CF, Latorre-Muro P, Puigserver P. Mechanisms of mitochondrial respiratory adaptation. Nat Rev Mol Cell Biol 2022;23(12):817–35.
[31] Lim MMK, Wee JWK, Soong JC, Chua D, Tan WR, Lizwan M, et al. Targeting metabolic flexibility via angiopoietin-like 4 protein sensitizes metastatic cancer cells to chemotherapy drugs. Mol Cancer 2018;17(1):152.
[32] Zhu P, Tan MJ, Huang RL, Tan CK, Chong HC, Pal M, et al. Angiopoietin-like 4 protein elevates the prosurvival intracellular O2(-):H2O2 ratio and confers anoikis resistance to tumors. Cancer Cell 2011;19(3):401–15.
[33] Pan CW, Jin X, Zhao Y, Pan Y, Yang J, Karnes RJ, et al. AKT-phosphorylated FOXO1 suppresses ERK activation and chemoresistance by disrupting IQGAP1-MAPK interaction. EMBO J 2017;36(8):995–1010.
[34] Jin X, Pan Y, Wang L, Ma T, Zhang L, Tang AH, et al. Fructose-1,6-bisphosphatase Inhibits ERK activation and bypasses gemcitabine resistance in pancreatic cancer by blocking IQGAP1-MAPK interaction. Cancer Res 2017;77(16):4328–41.
[35] Mehnert JM, Tan AR, Moss R, Poplin E, Stein MN, Sovak M, et al. Rationally designed treatment for solid tumors with MAPK pathway activation: a phase I study of paclitaxel and bortezomib using an adaptive dose-finding approach. Mol Cancer Ther 2011;10(8):1509–19.
[36] Okano J, Rustgi AK. Paclitaxel induces prolonged activation of the Ras/MEK/ERK pathway independently of activating the programmed cell death machinery. J Biol Chem 2001;276(22):19555–64.
[37] Ritt DA, Abreu-Blanco MT, Bindu L, Durrant DE, Zhou M, Specht SI, et al. Inhibition of Ras/Raf/MEK/ERK pathway signaling by a stress-induced phospho-regulatory circuit. Mol Cell 2016;64(5):875–87.
[38] Sun Q, Arnold RS, Sun CQ, Petros JA. A mitochondrial DNA mutation influences the apoptotic effect of statins on prostate cancer. Prostate 2015;75(16):1916–25.
[39] Lee JS, Lee H, Jang H, Woo SM, Park JB, Lee SH, et al. Targeting oxidative phosphorylation reverses drug resistance in cancer cells by blocking autophagy recycling. Cells 2020;9(9).
[40] Fiori ME, Di Franco S, Villanova L, Bianca P, Stassi G, De Maria R. Cancer-associated fibroblasts as abettors of tumor progression at the crossroads of EMT and therapy resistance. Mol Cancer 2019;18(1):70.
[41] Wang H, Li N, Liu Q, Guo J, Pan Q, Cheng B, et al. Antiandrogen treatment induces stromal cell reprogramming to promote castration resistance in prostate cancer. Cancer Cell 2023;41(7):1345–62 e9.
[42] Jia D, Zhou Z, Kwon OJ, Zhang L, Wei X, Zhang Y, et al. Stromal FOXF2 suppresses prostate cancer progression and metastasis by enhancing antitumor immunity. Nat Commun 2022;13(1):6828.
[43] Lang J, Zhao X, Qi Y, Zhang Y, Han X, Ding Y, et al. Reshaping prostate tumor microenvironment to suppress metastasis via cancer-associated fibroblast inactivation with peptide-assembly-based nanosystem. ACS Nano 2019;13(11):12357–71.
[44] Yeh CR, Slavin S, Da J, Hsu I, Luo J, Xiao GQ, et al. Estrogen receptor alpha in cancer associated fibroblasts suppresses prostate cancer invasion via reducing CCL5, IL6 and macrophage infiltration in the tumor microenvironment. Mol Cancer 2016;15:7.
[45] Civenni G, Bosotti R, Timpanaro A, Vazquez R, Merulla J, Pandit S, et al. Epigenetic control of mitochondrial fission enables self-renewal of stem-like tumor cells in human prostate cancer. Cell Metab 2019;30(2):303–18 e6.
[46] Humpton TJ, Alagesan B, DeNicola GM, Lu D, Yordanov GN, Leonhardt CS, et al. Oncogenic KRAS Induces NIX-mediated mitophagy to promote pancreatic cancer. Cancer Discov 2019;9(9):1268–87.
[47] Delaunay S, Pascual G, Feng B, Klann K, Behm M, Hotz-Wagenblatt A, et al. Mitochondrial RNA modifications shape metabolic plasticity in metastasis. Nature 2022;607(7919):593–603.
[48] Ippolito L, Morandi A, Taddei ML, Parri M, Comito G, Iscaro A, et al. Cancer-associated fibroblasts promote prostate cancer malignancy via metabolic rewiring and mitochondrial transfer. Oncogene 2019;38(27):5339–55.
[49] Fernandez-Hernando C, Suarez Y. ANGPTL4: a multifunctional protein involved in metabolism and vascular homeostasis. Curr Opin Hematol 2020;27(3):206–13.
[50] Jabs M, Rose AJ, Lehmann LH, Taylor J, Moll I, Sijmonsma TP, et al. Inhibition of endothelial notch signaling impairs fatty acid transport and leads to metabolic and vascular remodeling of the adult heart. Circulation 2018;137(24):2592–608.
[51] Hata S, Nomura T, Iwasaki K, Sato R, Yamasaki M, Sato F, et al. Hypoxia-induced angiopoietin-like protein 4 as a clinical biomarker and treatment target for human prostate cancer. Oncol Rep 2017;38(1):120–8.
[52] Xiao S, Nai-Dong W, Jin-Xiang Y, Long T, Xiu-Rong L, Hong G, et al. ANGPTL4 regulate glutamine metabolism and fatty acid oxidation in nonsmall cell lung cancer cells. J Cell Mol Med 2022;26(7):1876–85.
[53] Huang RL, Teo Z, Chong HC, Zhu P, Tan MJ, Tan CK, et al. ANGPTL4 modulates vascular junction integrity by integrin signaling and disruption of intercellular VE-cadherin and claudin-5 clusters. Blood 2011;118(14):3990–4002.
[54] Avalle L, Raggi L, Monteleone E, Savino A, Viavattene D, Statello L, et al. STAT3 induces breast cancer growth via ANGPTL4, MMP13 and STC1 secretion by cancer associated fibroblasts. Oncogene 2022;41(10):1456–67.
[55] Bajwa P, Kordylewicz K, Bilecz A, Lastra RR, Wroblewski K, Rinkevich Y, et al. Cancer-associated mesothelial cell-derived ANGPTL4 and STC1 promote the early steps of ovarian cancer metastasis. JCI Insight 2023;8(6).
[56] Choi M, Mukherjee S, Yun JW. Anthocyanin oligomers stimulate browning in 3T3-L1 white adipocytes via activation of the beta3-adrenergic receptor and ERK signaling pathway. Phytother Res 2021;35(11):6281–94.